Simulation of Synoptic- and Subsynoptic-Scale Phenomena Associated with the East Asian Summer Monsoon Using a High-Resolution GCM

NGAR-CHEUNG LAU AND JEFFREY J. PLOSHAY

NOAA/Geophysical Fluid Dynamics Laboratory, Princeton University, Princeton, New Jersey

ABSTRACT

A 20-yr simulation using a global atmospheric general circulation model with a resolution of 0.5° latitude × 0.625° longitude is compared with observational findings. The primary goal of this survey is to assess the model performance in reproducing various summertime phenomena related to the continental-scale Asian monsoon in general, and the regional-scale East Asian monsoon in particular. In both model and observed atmospheres, the seasonal march of the precipitation centers associated with the Asian summer monsoon is characterized by onsets occurring earliest over the southeastern Bay of Bengal, followed by rapid northeastward advances over Indochina, the South China Sea–Philippine Sea and the western Pacific, northward evolution in the East Asian sector, as well as northwestward development over the Bay of Bengal, the Indian subcontinent, and the Arabian Sea. This onset sequence is accompanied by southwesterly low-level flows over the rainy regions, as well as northwestward migration of the 200-mb Tibetan anticyclone. Analysis of the heat sources and sinks in various regions illustrates the prominent role of condensational heating in the local energy budget during the mature phases of monsoon development. In accord with observations, the simulated monsoon rains in the East Asian sector are organized about zonally elongated "mei-yu–baiu" (plum rain) systems. These precipitation features advance to higher latitudes during the June–July period, in conjunction with displacements of the axis of the low-level anticyclone over the subtropical western Pacific. A detailed case study is performed on a prominent rainy episode in the simulation. The model is capable of reproducing the observed intense gradients in temperature, humidity, and moist static stability in the vicinity of the mei-yu–baiu front, as well as the spatial relationships between the rainband and the three-dimensional flow field. The axis of the mei-yu–baiu rainband in this event is aligned with the trajectory of a succession of mesoscale cyclonic vortices, which originate from southwestern China and travel northeastward over the Yangtze River basin.

1. Introduction

The Asian monsoon (AM) is noted for both its large spatial extent and its strong intensity. This circulation system exerts profound impacts on socioeconomic activities of the dense population centers in that region (e.g., see Gadgil and Rupa Kumar 2006), as well as on climatic conditions throughout the globe (e.g., see Trenberth et al. 2006). The phenomena associated with the AM encompass a broad range of spatial and temporal scales. These monsoonal features are strongly influenced by the local orography and land–sea configuration, and thus exhibit a notable geographical dependence. Broadly speaking, the overall AM system could be viewed as a mosaic of several components prevailing in different portions of tropical and subtropical Asia. These subregions include South Asia, East Asia, the western North Pacific, and the Maritime Continent. The climatological seasonal evolution and the structural properties of the weather-scale disturbances residing in each of these sectors bear rather distinct characteristics. In addition, there exist considerable interactions among the monsoon flows in different subregions. Therefore a full understanding of the AM must take into account the multiscale aspects of a wide variety of phenomena and processes.

In the past decades, much progress has been made in the study of the East Asian Summer Monsoon (EASM). This particular component of the AM is a strong determinant of the climates in China, Japan, and Korea during the warm season. Principal findings on

Corresponding author address: Ngar-Cheung Lau, NOAA/ Geophysical Fluid Dynamics Laboratory, Princeton University, Forrestal Campus, P.O. Box 308, Princeton, NJ 08542.
E-mail: gabriel.lau@noaa.gov

the climatological and time-varying facets of the EASM have recently been summarized in the monograph edited by Chang (2004), the review article by Ding and Chan (2005), and several chapters in another monograph edited by Wang (2006). These publications provide ample evidence on the unique nature of the monsoonal circulation systems in East Asia, and the intricate relationships between the EASM and features occurring in other subregions of the AM complex.

Experiments have been conducted at many research centers to simulate various facets of the AM using general circulation models (GCMs), with typical horizontal resolutions of 2°–5° of latitude and longitude. The performance of this class of models in reproducing the basic monsoon characteristics and the impacts of El Niño on monsoon intensity has been summarized by Sperber et al. (1994), Sperber and Palmer (1996), Lau et al. (1996), Kang et al. (2002), Kang (2004), and Wang et al. (2004), among others. Some of these model intercomparison studies have assessed the effects of model resolution on the monsoon simulations. As can be expected, synoptic- and subsynoptic-scale features are not well simulated in GCMs with resolutions lower than ~200 km. Of particular note is the inadequate representation in such models of the observed rainbands accompanying the northward advance of the EASM over China, Japan, Korea, and the nearby waters (Lau et al. 1996; Kang 2004). On the other hand, a model with higher resolution (~100 km) is seen to capture this important phenomenon (Sperber et al. 1994). It is evident from these studies that models with much increased spatial resolution would enhance our capability to simulate the details of various monsoon systems of interest, and thereby expand our knowledge of the mechanisms governing the formation and development of such features.

Pursuant to the advances in computer technology and numerical model design, it is currently feasible to perform extended integrations using global GCMs with resolutions higher than ~50 km. It is anticipated that these high-definition models would serve as valuable tools for projecting and understanding the influences of global modes of variability (such as El Niño–Southern Oscillation) and long-term trends (such as greenhouse warming) on regional climates with progressively finer spatial scales. Climate simulations based on these high-resolution global models have been conducted and analyzed at various centers. Results of such experiments have been reported by Branković and Gregory (2001) for the European Centre for Medium-Range Weather Forecasts (ECMWF) model (0.56° grid), Duffy et al. (2003) for the National Center for Atmospheric Research (NCAR) Community Climate Model, version 3

(CCM3) model (55-km grid), Ohfuchi et al. (2004) for the Earth Simulator model (10-km grid), Mizuta et al. (2006) for the Japan Meteorological Agency model (20-km grid), and Roeckner et al. (2006) for the ECHAM5 model (0.75° grid) at the Max Planck Institute for Meteorology. Some of these studies demonstrate that increased model resolution leads to more realistic simulations. Such improvements are particularly evident in the representation of orographic effects and various physical processes. However, other results (Branković and Gregory 2001) indicate that enhanced model resolution does not always yield a better comparison with observations, and that appropriate physical parameterization schemes need to be developed for the high-resolution models.

In recent years, considerable resources have been devoted to the development of, and experimentation with, high-resolution models at the Geophysical Fluid Dynamics Laboratory (GFDL). Output from multidecadal runs based on these models is now available for analysis. The primary goal of the present study is to evaluate the capability of one version of such models to simulate the essential atmospheric phenomena associated with the EASM. We have selected this specific monsoon system as a focus of our model diagnosis in view of its multiscale nature, and the continued interest of the research community in the climate of this region, as noted in the above discussions. The myriad circulation systems related to EASM, with spatial scales extending from less than 100 km to 1000 km and beyond, and with temporal scales ranging from hours to the annual cycle, constitute a rich test bed for assessing the performance of high-resolution GCMs. This evaluation is further facilitated by the considerable knowledge base for the EASM, as established by the multitude of observational analyses on this subject.

The specifications of the GCM to be examined in this study, and the observational datasets used for validating the model output, are described in section 2. Our diagnosis begins in section 3 with a comparison of the summer monsoon climatology of this particular model with corresponding simulations of other model versions with various resolutions and modes of air–sea interaction, followed by a description of the detailed evolution of the AM system during the summer season, and the evolution of the principal heat sources and sinks. The climatological development of the major precipitation and circulation systems during the onset and establishment phases of the EASM is analyzed in section 4. Much attention of this work is devoted to the detailed characteristics of an outstanding episode of rain-producing weather systems accompanying the seasonal march of EASM in the model atmosphere. The princi-

pal findings of this investigation are reported in section 5. The article concludes with a summary and discussion in section 6.

2. Model specifications and observational datasets

The model being analyzed in this study is a global atmospheric GCM developed at GFDL. The dynamical core of this model is constructed by Lin (2004), and uses a finite-volume formulation with a terrain-following Lagrangian control-volume discretization. The horizontal resolution of the primary model version examined here is 0.5° latitude × 0.625° longitude. This version is labeled as M180, where "180" refers to the number of grid points between the equator and the Pole. The suite of physical processes incorporated in this model is similar to that described by the GFDL Global Atmospheric Model Development Team (2004). These processes include radiative transfer, cloud formation, convection, fluxes across the lower boundary, turbulence within the boundary layer, gravity wave drag, and ground hydrology. In particular, moist convection is parameterized using the relaxed Arakawa–Schubert scheme as described in Moorthi and Suarez (1992). There are 24 atmospheric layers in the vertical direction, with 9 levels being located within 1.5 km from the lower boundary, and 5 levels within the stratosphere. Most of the results to be presented in the following sections are based on a 20-yr integration of the M180 model. When launched on an array of 90 Origin MIPS processors, approximately 24 h of wall clock time are needed to complete the integration for one model year. The climatological seasonal cycle of observed sea surface temperature (SST) is prescribed at ocean grid points, so that the SST boundary forcing does not vary from year to year during the model integration. The SST conditions used in this experiment are based on averages of the optimal interpolation analyses (version 1) over the 1981–99 period, as documented by Reynolds et al. (2002). The horizontal resolution of this dataset is 1° latitude and longitude. Monthly mean SST values are set at the middle of each month, and variations at 12-hourly intervals are obtained by linear interpolation between these values for adjacent months.

The dependence of some of the climatological results on model resolution is assessed by contrasting the simulation using the M180 grid with results based on versions with latitude–longitude resolutions of 2° × 2.5° (M45), 1° × 1.25° (M90), and 0.25° × 0.3125° (M360). The latter integrations are also conducted using climatological SST boundary forcing. The duration of these model runs is 20 yr for M45 and M90, and 5 yr for M360. The impacts of air–sea interaction on the model

climatology are examined using the output from two 20-yr integrations with a coupled GCM (CM 2.1), which is described in Delworth et al. (2006). In the first (second) integration, the atmospheric component of CM2.1 has the same formulation and resolution as the M45 (M90) models mentioned above. These coupled models will be referred as the CM2.1-M45 and CM2.1-M90, respectively. As the model resolution is increased from M45 to M360, changes are made to various physical and numerical parameters, including enhanced Rayleigh friction at the top model level, strengthened gravity wave drag, and a shortened time step.

Whenever feasible, the model climatological fields to be displayed in sections 3–4 are compared against the corresponding observations. The observed geopotential height and wind fields are based on long-term averages of the reanalysis data produced by the ECMWF for the 1958–2002 period (Uppala et al. 2005). This dataset, hereafter referred to as the 40-yr ECMWF Re-Analysis (ERA-40), has a horizontal resolution of 1.1° latitude and longitude. Observational estimates of the precipitation field are derived from the data collected at satellite-mounted radar platforms during the Tropical Rainfall Measuring Mission (TRMM; see Kummerow et al. 2000), which extends over the 9-yr period from 1998 to 2006. The TRMM dataset being examined in this study is the 3B42 version 6, which is compiled by blending passive microwave measurements collected at various TRMM sensors with infrared soundings taken by the international constellation of geostationary satellites (Huffman et al. 2007). This dataset, which has a latitudinal and longitudinal resolution of 0.25°, is selected by virtue of the lower-level spatial noise due to the large data sample sizes used in estimating the precipitation intensity (e.g., see Kikuchi and Wang 2008).

3. Asian summer monsoon—Continental-scale aspects

We begin our presentation by placing the performance of the M180 model in the context of the summer monsoon simulations by a broad range of model tools currently available at GFDL. The climatological patterns of precipitation (shading) and 850-mb wind vector (arrows) for the June–August season are displayed in Fig. 1 for (Fig. 1a) TRMM and ERA-40 data, and for the (Fig. 1b) M360, (Fig. 1c) M180, (Fig. 1d) M90, (Fig. 1e) M45, (Fig. 1f) CM2.1-M90, and (Fig. 1g) CM2.1-M45 models. These results are based on averages over 9 and 45 yr for the TRMM and ERA-40 data, respectively, 5 yr for M360, and 20 yr for all other models (see section 2 for details).

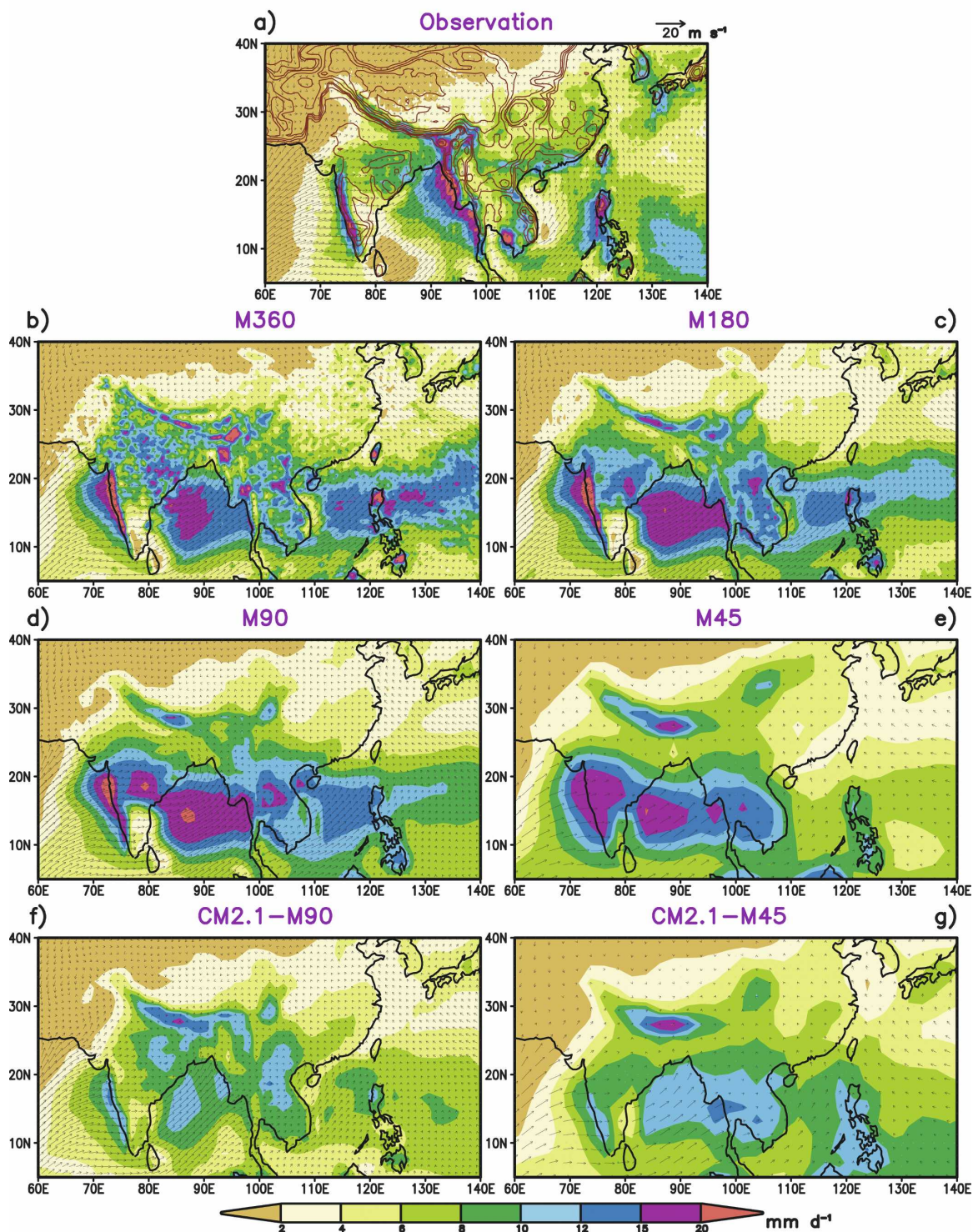## Precipitation/surface winds (JJA)

FIG. 1. Distributions of the long-term-averaged precipitation rate (shading, see scale at bottom) and surface wind vector (arrows, see scale at upper right) for the June–August season. Results are based on (a) TRMM/ERA-40 data, and simulations by the (b) M360, (c) M180, (d) M90, (e) M45, (f) CM2.1-M90, and (g) CM2.1-M45 models. Dark red contours in (a) indicate orographic heights (shown for 250, 500, 750, 1000, 2000, 3000, 4000, and 5000 m). All precipitation patterns are plotted at full resolution of the corresponding dataset. The wind vectors for (d) M90, (e) M45, (f) CM2.1-M90, and (g) CM2.1-M45 are also shown using full resolution. For the sake of clarity, the arrows in the (b) M360 and (c) M180 patterns are plotted at M90 resolution (i.e., by using the wind data at every second and every fourth grid point, respectively, in both longitudinal and latitudinal directions).

The observed rainfall pattern during the summer season (Fig. 1a) is characterized by precipitation maxima over the western coast and the northern portion of the Indian Subcontinent, the western coast of the Indochina Peninsula and nearby waters in the Bay of Bengal, the eastern portion of Indochina, the eastern portion of the South China Sea, and the subtropical western Pacific. These rainy regions are mostly situated on the windward side of the local terrain (note the relationship between the prevalent southwesterly surface flows and the major orographic features, as depicted by dark red contours in Fig. 1a). Conversely, the prominent dry zones in southeastern India and the southwestern portion of the Bay of Bengal, the central portion of Indochina, and the waters off the eastern coast of Vietnam are located on the leeward side of the mountain barriers. The dryness off the Vietnamese coast are also partially attributed to the cold SST conditions in that region, which are in turn associated with coastal upwelling induced by the alongshore component of the southwesterly summer monsoon. Low-level anticyclonic vorticity of the mean flow environment over some parts of the southwestern Bay of Bengal (not shown) might contribute to the dry conditions in that region. This vorticity pattern is mainly determined by the meridional shear of the zonal flow (i.e., $-\partial u/\partial y$).

For the atmospheric GCMs, the contrasts between the wet and dry regions as noted in Fig. 1a are not well simulated in the M45 version (Fig. 1e), but become progressively more evident as the model resolution is increased (see Figs. 1b–d). Various small-scale details, such as the precipitation centers along the southern foothills of the Tibetan Plateau and over the northern Philippines, are also more realistic in the models with higher resolution.

All atmospheric GCMs (Figs. 1b–e) produce too much rainfall over the subtropical western Pacific near 20°N and the Bay of Bengal. The positive precipitation bias in the western Pacific sector is particularly strong in the M360 version, and is locally accompanied by excessive cyclonic surface flows in that simulation (see Fig. 1b). The rainfall rates over the subtropical western Pacific near 20°N and Bay of Bengal in the simulations by the coupled GCMs (Figs. 1f,g) are mostly lower than those produced by atmospheric GCMs of comparable resolution (Figs. 1d,e). These results suggest that the overestimation of precipitation in these regions by the atmospheric GCMs may partially be attributed to the absence of two-way air–sea coupling in these models. The SST field in the subtropical western Pacific and Bay of Bengal, as prescribed in the atmospheric GCM simulations, is seen to be warmer than the corresponding SST field simulated in the coupled GCMs by ap-

proximately 0.5°–1.5°C (results not shown). The relatively heavier precipitation in the atmospheric GCM runs is in accord with such differences in the local SST conditions. The feedbacks between SST and convection in the Asian monsoon region, and their implications on the local and remote circulation, have been examined by Fu et al. (2002) using both air–sea coupled and stand-alone atmospheric GCMs. Copsey et al. (2006) have also noted that the response of atmospheric GCMs to prescribed SST forcing in the Indian Ocean may not provide a full description of the atmosphere–ocean interactions in that region. Whereas the CM2.1 yields a better simulation of the rain intensity over some maritime areas, other regional features (e.g., the narrow precipitation zone near the Western Ghats of India) are less well represented in the simulations by the coupled model than by the atmospheric GCM. We shall henceforth devote our attention to the simulation by the M180 model, since it has adequate resolution for defining various mesoscale monsoon features of interest (also see review in section 1 of previous studies on impacts of model resolution), and the duration of the integration with this version (i.e., 20 yr) is sufficiently long to compile a stable model climatology.

The evolution of the AM through the first half of the summer season is illustrated in more detail in Fig. 2, which shows the long-term-averaged distributions of precipitation (shading) and 200-mb height (contours) for the M180 model (Figs. 2a–d), and for the TRMM and ERA-40 data (Figs. 2e–h). Patterns are displayed for consecutive 10-day periods in the climatological calendar, starting with 21–30 May, and ending with 20–29 June.

In the model atmosphere, the arrival of the rainy season is marked by the onset of intense rainfall over Andaman Sea (southeastern Bay of Bengal), the Gulf of Thailand, and the surrounding land areas as early as 21–30 April (results not shown). The heaviest precipitation advances toward the southern portion of the Indochina Peninsula and the nearby waters, as well as the southern tip of the Indian Subcontinent during the 21–30 May period (Fig. 2a). These precipitating zones spread northward, westward, and eastward during the following month (Figs. 2b–d). By the end of June (Fig. 2d), intense precipitation is generated over most parts of the South China Sea and Bay of Bengal, the northeastern portion and western coast of India, the southern edge of the Tibetan Plateau, and the subtropical western Pacific. In the eastern part of the AM region, an elongated rainbelt extending northeastward from southwestern China (near 22°N, 110°E) to southern Japan (near 35°N, 140°E) is simulated in mid-June (Fig. 2c).
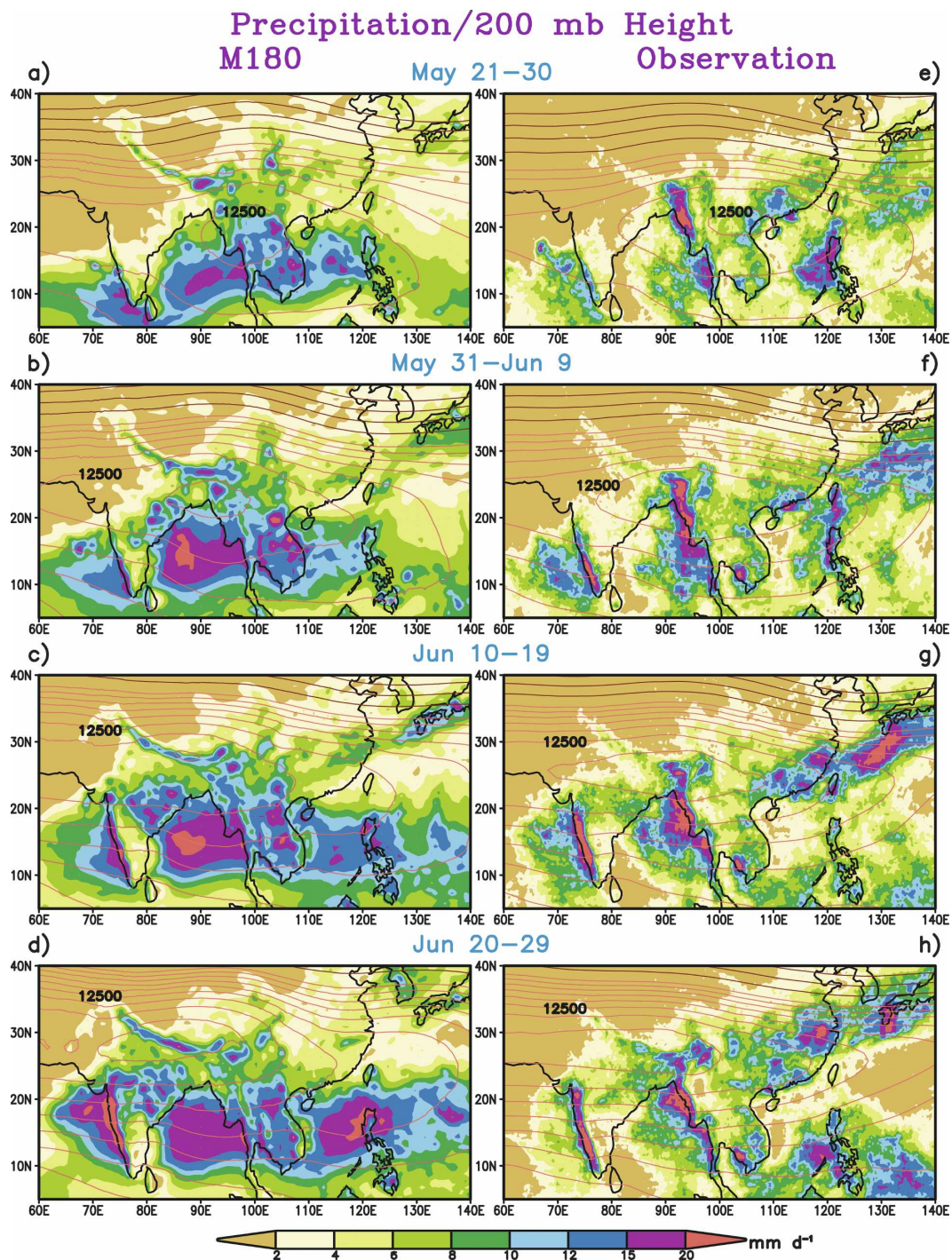
Precipitation/200 mb Height

FIG. 2. Distributions of the long-term-averaged precipitation rate (shading, see scale at bottom) and 200-mb height (contours), for the 10-day periods of (a), (e) 21–30 May; (b), (f) 31 May–9 Jun; (c), (g) 10–19 Jun; and (d), (h) 20–29 Jun as computed using (a)–(d) M180 output and (e)–(h) TRMM/ERA-40 data. Red and purple contours indicate values of 200-mb height above and below 12 400 m, respectively. Interval (CI): 20 m for red contours; 50 m for purple contours.

A distinct anticyclonic center is simulated at 200 mb over the Indochina Peninsula in late May (see contours in Fig. 2a). This feature is almost collocated with the precipitation maximum in that region. In conjunction with the subsequent northward and westward development of the principal precipitation zones, this high center follows a migratory path with a similar orientation, and arrives at the southern Tibetan Plateau in late June (Fig. 2d). The intensity of this anticyclone also increases during this period.

Several facets of the spatiotemporal evolution of the simulated monsoon features, as noted in the preceding paragraphs, are in fair agreement with the corresponding observations based on TRMM and ERA-40 data (Figs. 2e–h). Of particular note is the onset and intensification of the rainfall near the Western Ghats of India, as well as the northwestward movement of the amplifying high pressure center at 200 mb from Indochina to the Tibetan Plateau. There are, however, also considerable discrepancies between the rainfall climatology in the model and observed atmospheres. As already noted in the discussion of Fig. 1, the observed east–west contrast in precipitation over the South China Sea and Bay of Bengal is much less evident in the model simulation. The heavy precipitation observed along the northwestern coast of the Indochina Peninsula through much of the late May–late June period is not adequately reproduced by the model. The simulated and observed patterns also differ in the timing of the poleward migration of the East Asian rainbelt stretching from southwestern China to southern Japan. The spatial coherence of this elongated precipitation feature is relatively stronger in the observational pattern than in the model atmosphere. We shall examine the characteristics of this rainband in greater detail in the next section.

Another perspective of the space–time development of the precipitation and low-level circulation associated with the major components of AM is offered in Fig. 3, which shows the distributions of precipitation (shading) and 850-mb horizontal wind vector (arrows) as a function of time (ordinate) and longitude (abscissa). These plots are based on averages over the zonal band between 12.5° and 22.5°N, and are computed using (Fig. 3a) M180 and (Fig. 3b) TRMM/ERA-40 data. The model pattern (Fig. 3a) illustrates that, in accord with the evidence presented in Figs. 1–2, the AM system consists of five main components, which are situated over western India–Arabian Sea (70°–75°E), western Indochina–Bay of Bengal (80°–100°E), central and eastern Indochina (100°–110°E), South China Sea (110°–125°E), and the western Pacific (125°–140°E). The earliest monsoon rains (with simulated precipita-

tion rates exceeding 10 mm day^{-1}) are seen to arrive at Indochina (near 100°E) in early May. This monsoon onset is followed by similar occurrences in the sectors corresponding to the Bay of Bengal (late May), the South China Sea (late May or early June), the western India–Arabian Sea (early June), and the western Pacific (mid-June to July). The principal precipitation signals in Fig. 3a are coincident with enhanced westerly or southwesterly flows at 850 mb. Prominent troughs (as indicated by counterclockwise turning of the wind vectors from west to east) are discernible to the west of the rainfall maxima over the Bay of Bengal and the South China Sea.

The relative timing of the monsoon onsets in various sectors and the relationships between the rainfall maxima and the ambient circulation, as inferred from the model output (Fig. 3a), are in broad agreement with the observations (Fig. 3b). The longitudinal extent of the individual precipitation zones in the observed pattern is narrower than that of the simulated features. The relatively dry zones (with precipitation rates less than 6 mm day^{-1}) near 80°, 100°, 110°, and 125°E, which separate the five major monsoon regions noted in the preceding paragraph, are more evident in the TRMM pattern than in the model simulation. These observed dry zones mostly correspond to the leeward side of mountain barriers (see Fig. 1a), or to the underlying cold SST condition (such as that due to coastal upwelling near 110°E).

The temporal evolution of the principal heat sources and sinks in six selected regions of the AM system is illustrated in Fig. 4. These regions correspond to the western Tibetan Plateau (region 1), the eastern Tibetan Plateau (region 2), the southern slope of the Tibetan Plateau (region 3), the northern Bay of Bengal and the surrounding land areas (region 4), Indochina (region 5), and southeastern China (region 6). The boundaries of all six regions are indicated in the map inserted between Figs. 4a and 4b (see figure caption for further details). Climatological means of the heat gain or loss within the entire atmospheric column above each region due to vertically averaged latent heat release, sensible heating at the lower boundary, and net (longwave and shortwave) radiative fluxes at the upper and boundaries are computed using M180 data for successive 10-day periods. The time series of these forcing terms in the vertically integrated heat budget for regions 1–6 are displayed in Fig. 4, with the values of the individual components being presented in a cumulative format along a column for each 10-day period. The sum of the three heating components is indicated using red dots linked to each other by short line segments.
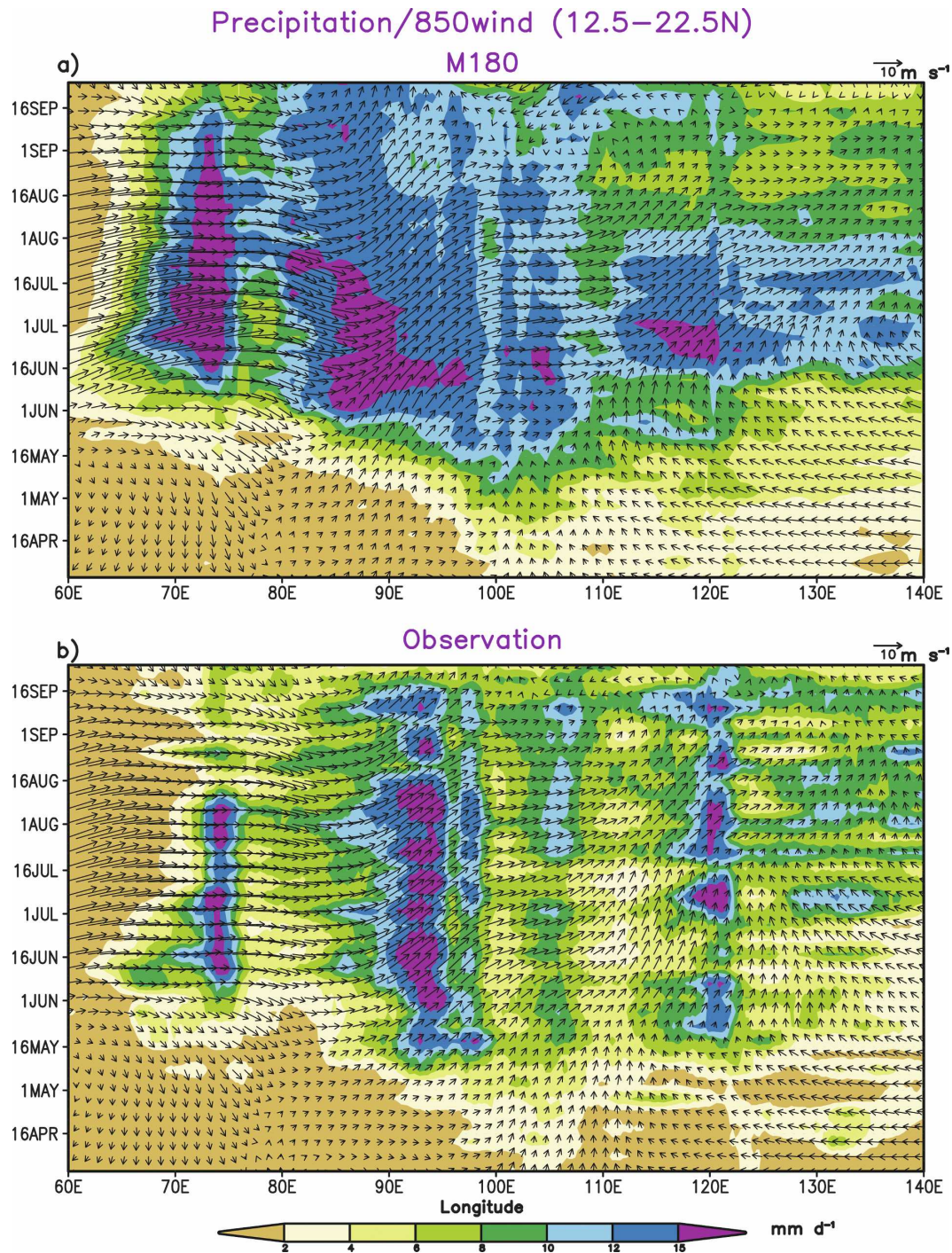
FIG. 3. Variations of the long-term-averaged precipitation rate (shading, see scale at bottom) and 850-mb horizontal wind vector (arrows, see scale at upper right) with lon (abscissa) and time (ordinate), as computed using (a) M180 output and (b) TRMM/ERA-40 data for various 5-day periods (pentads). All data are averaged over latitudes between 12.5° and 22.5°N.

The data plotted in Fig. 4 illustrate that condensational heating accompanying the monsoonal precipitation (as indicated by the green columns) is the dominant forcing term for regions 3–5 during the summer months, and for region 6 throughout the April–August period. The temporal lag of the evolution of latent heating over region 4 relative to that over region 5 is indicative of the northward and westward spread of the
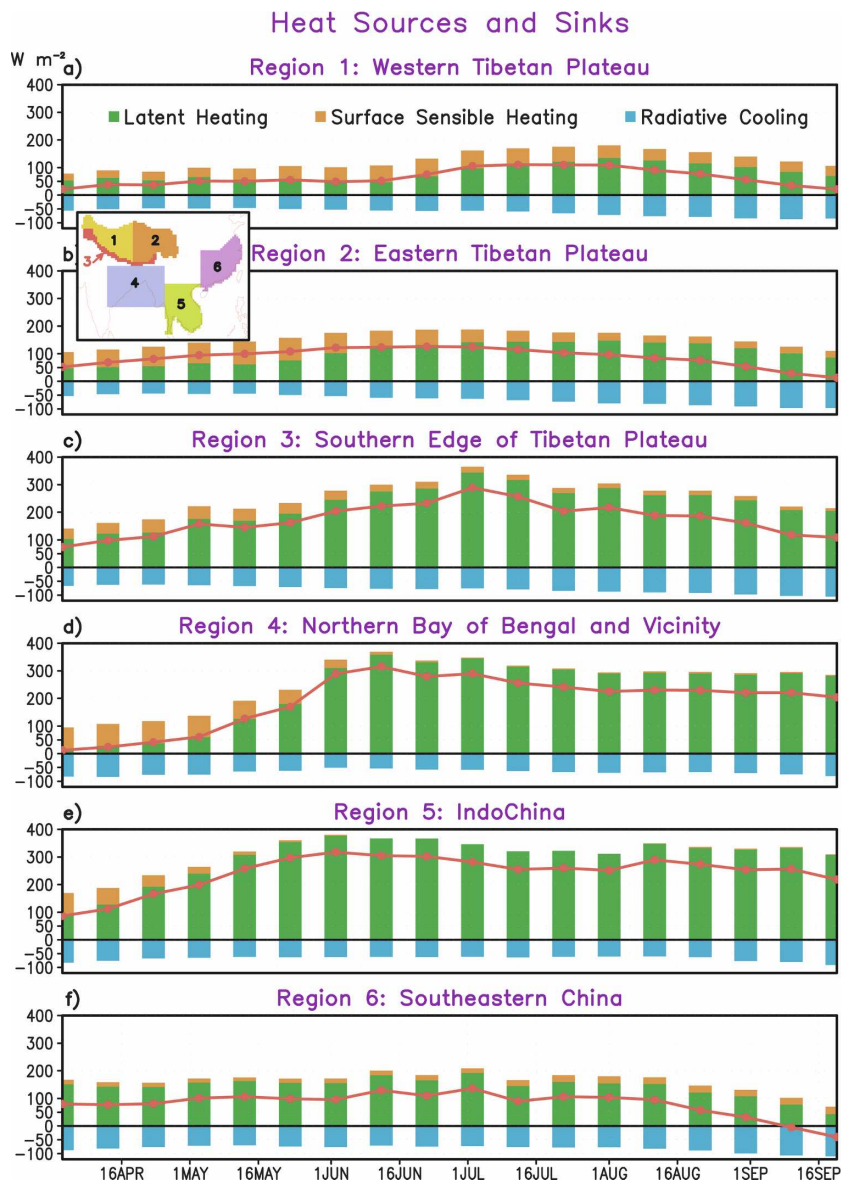
FIG. 4. Variations with time of the contributions of latent heat release (green columns), surface sensible heating (brown columns), and net radiative cooling (blue columns) to the vertically integrated heat balance of the atmospheric column over (a) region 1 (western Tibetan Plateau), (b) region 2 (eastern Tibetan Plateau), (c) region 3 (southern edge of Tibetan Plateau), (d) region 4 (northern Bay of Bengal and surrounding land areas), (e) region 5 (Indochina), and (f) region 6 (southeastern China). The sum of the three contributions is indicated using red dots connected by red line segments. The Tibetan Plateau corresponds to grid points higher than 4000 m, with the 87.5°E meridian being taken as the boundary between the eastern and western portions (regions 1 and 2, respectively). Region 3 is comprised of grid points on the southern edge of the plateau, with altitudes between 500 and 4000 m, and longitudes between 72.5° and 95°E. Region 4 is defined as the rectangular site situated between 16.5°–26.5°N and 80°–97.5°E. Region 5 consists of land points between 9°–22°N and 97.5°–110°E. Region 6 consists of land points in southeastern China between 108° and 122°E. The locations of regions 1–6 are shown in the inset map between (a) and (b). All data are based on long-term-averaged M180 output for successive 10-day periods.

monsoon rains from Indochina. The latent heating over both the western and eastern portions of the Tibetan Plateau (regions 1–2) is comparatively weaker than that over regions 3–5, and peaks in late July or early August. The latent heating over southeastern China (region 6) is stronger than that in regions 1–2, but weaker than that in regions 3–5.

The surface sensible heating (brown columns in Fig. 4) contributes significantly to the heat budget in regions 3–5 in April–May. The sensible heat source remains to be a substantial component of the heat source over the Tibetan Plateau (regions 1–2) through much of the warm season. The net radiative fluxes (blue columns) lead to a net heat loss over all six regions considered here, with relatively weak variations within the April–September period.

The magnitudes of the observed latent heating for the late May–early July period, as computed by Luo and Yanai (1984), are 58, 71, 273, and 208 W m^{-2} for regions 1, 2, 4, and 6, respectively. Observational values of radiative cooling (Katayama 1967; Yeh and Gao 1979; Nitta 1983) range from 60 to 90 W m^{-2} for all four regions. The observed sensible heating rate, as reported by Ueda et al. (2003), is 62 W m^{-2} for May in region 1 and 77 W m^{-2} for July in region 2. In many respects, the model results in Fig. 4 agree with the observational estimates cited above. The magnitude of the total diabatic heating in the model atmosphere (red dots in Fig. 4) also falls within the range of observational values presented in the aforementioned studies and in Yanai and Wu (2006). The latent heating in the simulated atmosphere over region 4 ($>$300 W m^{-2}) is stronger than the corresponding observational estimate (273 W m^{-2}; see Luo and Yanai 1984). This discrepancy is linked to the excessive precipitation generated in the model atmosphere over the Bay of Bengal and northeastern India (see Figs. 1–2).

4. Seasonal march of East Asian summer monsoon—Climatological aspects

The evolution of the climatological precipitation and circulation fields in the East Asian sector through the summer season is depicted in Fig. 5, which shows the variations of long-term means for rainfall rates (shading) and 850-mb horizontal wind vector (arrows) in different pentads (abscissa) and latitudes (ordinate). The values displayed here are based on averages of (Fig. 5a) M180 and (Fig. 5b) TRMM/ERA-40 data for longitudes ranging from 110°E (corresponding to the western South China Sea and western China) to 130°E (the Philippine Sea, the East China Sea, and western Japan).

In the model pattern (Fig. 5a), the earliest precipitation feature is simulated within the zone between 25° and 35°N during the April–May period. This phenomenon has been referred to as the "South China spring rain" by LinHo et al. (2008). The simulated spring rain period is followed by a succession of northward jumps of the precipitation centers. The overall timing of these jumps matches well with the northward and westward displacement of the precipitation centers and upper-level anticyclone over South Asia, as noted in the previous section. The primary rainfall maximum over East Asia, initially situated near 26°N in early June, is seen to migrate to 30°N in mid-June. It then advances rather abruptly to 36°–39°N in late June. Two additional leaps to 40°N (in mid-July) and 42°N (late July) are also discernible in Fig. 5a. Within the 15°–20°N zone, the sudden increase of simulated rainfall rates in late April–May is indicative of the monsoon onsets over the South China Sea.

Inspection of the vector pattern in Fig. 5a reveals that the enhanced rainfall during the South China spring rain period (April–May) and the sequence of sudden poleward jumps of precipitation centers (June–July) is coincident with strengthened southwesterly flows at 850 mb. The prevalent circulation equatorward of these southwesterly flows is distinctly anticyclonic, as can be inferred by the clockwise turning of the wind vectors for a given pentad when they are scanned from south to north. This configuration of the circulation in relation to the rainfall distribution implies that the precipitation maxima associated with the EASM are intimately linked to the location of the low-level subtropical anticyclone in that region. Poleward leaps of the precipitation centers are seen to be accompanied by corresponding shifts in the axis of the anticyclone.

The robustness of the principal features in Fig. 5a, which is based on 20-yr means of the M180 simulation, has been tested by making analogous plots using averages over four individual 5-yr segments of this model run. The latter patterns (not shown) confirm that the series of abrupt jumps of the precipitation maxima from about 25° to about 40°N during the June–July period, and the attendant displacement of the subtropical anticyclone, are highly reproducible throughout the course of the simulation. The timing of these northward jumps, as inferred from the model output for individual 5-yr segments, does not differ from the 20-yr climatological scenario (Fig. 5a) by more than 10 days. This notable tendency for phase locking of the East Asian rainfall development in individual summers with the annual cycle is reminiscent of the phenomena associated with climatological intraseasonal oscillations (e.g., see Wang and Xu 1997). Plots similar to Fig. 5a have
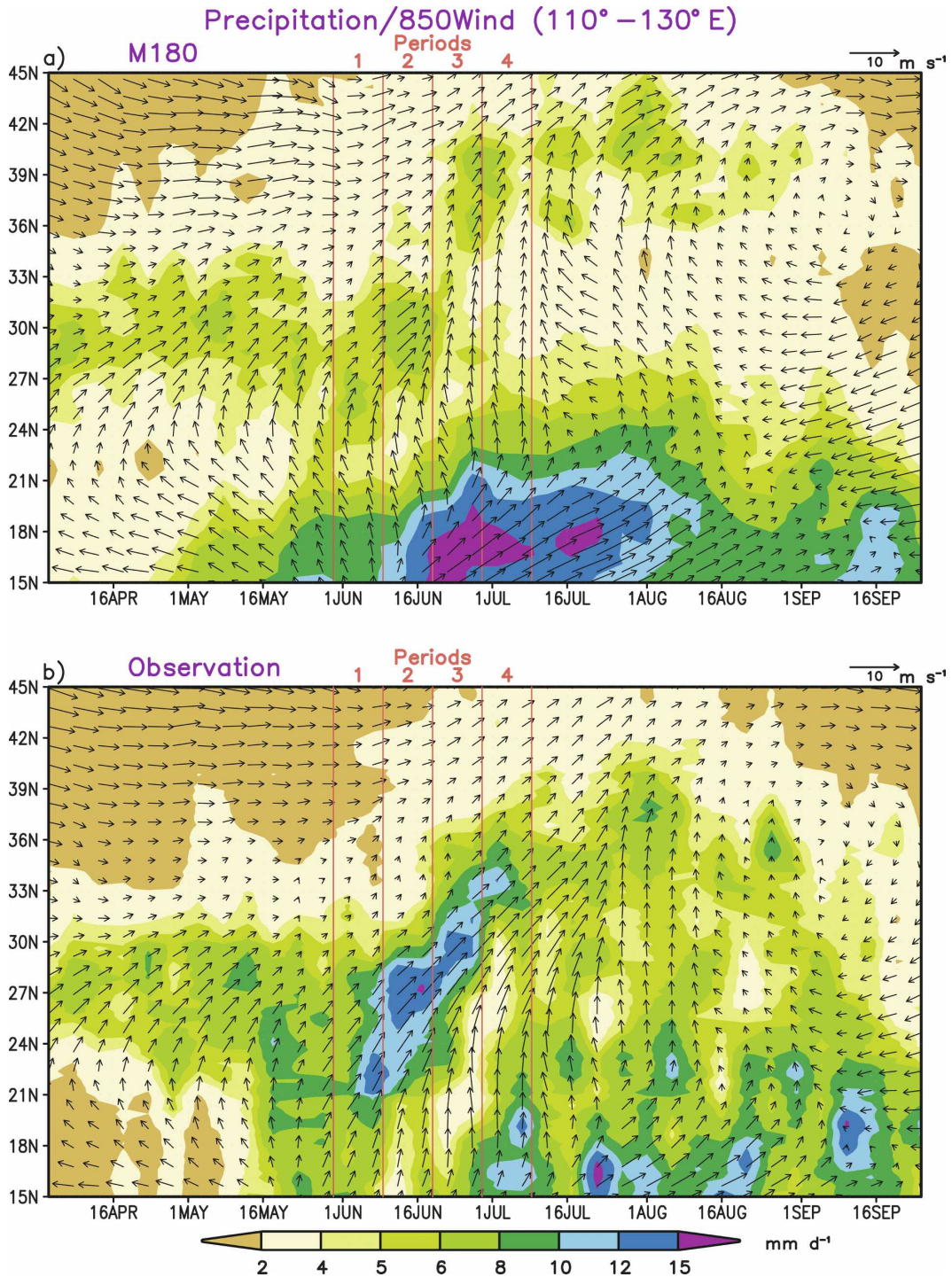
FIG. 5. Variations of the long-term-averaged precipitation rate (shading, see scale at bottom) and 850-mb horizontal wind vector (arrows, see scale at upper right) with time (abscissa) and lat (ordinate), as computed using (a) M180 output and (b) TRMM/ERA-40 data for various 5-day periods (pentads). All data are averaged over longitudes between 110° and 130°E. Vertical red lines indicate the 10-day ranges of periods 1–4 examined in Fig. 6.

also been constructed using outputs from integrations based on the various model versions presented in Fig. 1. These results (not shown) indicate that the northward jumps of the rainbelt in East Asia are simulated by these model versions to varying extents. Among the atmospheric models, this phenomenon is more evident as the model resolution increases. The precipitation jumps are generally more discernible in the atmospheric models than in the coupled models.

The northward migration of the monsoon rains from 20° to 40°N in June–July has been noted in the observational literature (e.g., see reviews by Lau and Li 1984; Lau et al. 1988). The stepwise character and abruptness of the simulated precipitation shifts are less evident in the TRMM data (Fig. 5b). However, the corresponding pattern based on independent observational rainfall data in the East China sector (110°–120°E), as presented by Ding (2004, see his Fig. 21), does support the existence of successive poleward jumps in the precipitation centers in that region. The precipitation intensity of this poleward-migrating feature, as inferred from the TRMM data (Fig. 5b), is higher than that in the model pattern (Fig. 5a). The observed migration ends at about 40°N; whereas the simulated precipitation centers reach as far north as 45°N. The spatial relationships between the principal precipitation features and the 850-mb circulation, as noted in the model atmosphere, are also evident in Fig. 5b.

To gain a better appreciation of the geographical patterns of the precipitation and circulation fields in various stages of monsoon development in East Asia, the spatial distributions of long-term averaged rainfall rates (shading) and 850-mb streamlines for four consecutive 10-day periods are presented in Fig. 6 using M180 data (Figs. 6a–d) and TRMM/ERA-40 data (Figs. 6e–h). We shall hereafter refer to the 10-day intervals used in constructing these charts as period 1 (31 May–9 June), period 2 (10–19 June), period 3 (20–29 June) and period 4 (30 June–9 July). The temporal extent of periods 1–4 is indicated in Fig. 5 using vertical red lines.

The most prominent feature in the simulated climatological precipitation pattern in period 1 (Fig. 6a) is the elongated maximum stretching northeastward from southwestern China to the East China Sea and the waters south of Japan. The enhanced rainfall in this region during late spring and early summer is referred to as "plum rain" (or "mei-yu" and "baiu" in Chinese and Japanese, respectively) by local meteorologists. In period 2 (Fig. 6b), increases in the simulated precipitation intensity are noted over the Yangtze River basin in central China (near 30°N) and over western Japan. In periods 3–4 (Figs. 6c,d), heavy rainfall arrives at the Yellow Sea, the Korean Peninsula (referred locally as

the "Changma" episode), the Sea of Japan, and central Japan. This sequence of jumps of the precipitation centers over East Asia contributes to the appearance in Fig. 5a of the northward movement of rainfall maxima in a succession of distinct steps.

The simulated summertime circulation over East Asia is strongly influenced by the low-level anticyclone over the subtropical western Pacific (see streamlines in Figs. 6a–d). In period 1 (Fig. 6a), the axis of this anticyclone is slanted northeastward from about 22°N, 120°E to 28°N, 150°E. Through the following month, the western portion of this ridge axis swings northward, so that, by period 4 (Fig. 6d), the anticyclone develops a northwest-to-southeast tilt from about 35°N, 125°E to 30°N, 150°E. In each of the 10-day periods described in Fig. 6, the heaviest precipitation is situated to the northwest of this anticyclone, and is connected to the moisture sources over South and East China Seas by southwesterly or southerly flows. In contrast, the rainfall rates near the axis of the anticyclone are much lower.

The essential characteristics of the evolution of the mei-yu–baiu rainband and the attendant circulation pattern are supported by the observations (Figs. 6e–h). For a given location, the arrival date of the simulated precipitation associated with mei-yu–baiu is about 10 days earlier than observed. In period 1 (Fig. 6e), the observed mei-yu–baiu rainband extends northeastward from about 20°N, 115°E to 30°N, 150°E. This feature remains to be distinguishable throughout its northward journey from South to North China. On the other hand, the corresponding feature in the model atmosphere is relatively weaker in periods 3–4 (Figs. 6c,d).

5. Temporal development and spatial structure of the mei-yu–baiu system—A case study

a. Synoptic features

To search for scenarios of robust and well-defined synoptic development that is sustained for at least 3–4 days, charts of precipitation and 850-mb streamlines for outstanding rainy events occurring throughout the 20-yr integration are examined. Among the strong episodes thus identified, the specific case to be described in this section exhibits some of the most intense precipitation and circulation signals that remain coherent through a week-long period. This event occurs in mid-June of year 3 of the simulation.

The distributions of the precipitation (shading) and 850-mb streamlines in the model atmosphere for each day of the 11–16 June period of year 3 are shown in Fig. 7. On 11 June (Fig. 7a), two separate precipitation maxima are seen over western and southwestern China. Each of these features is associated with a distinctive
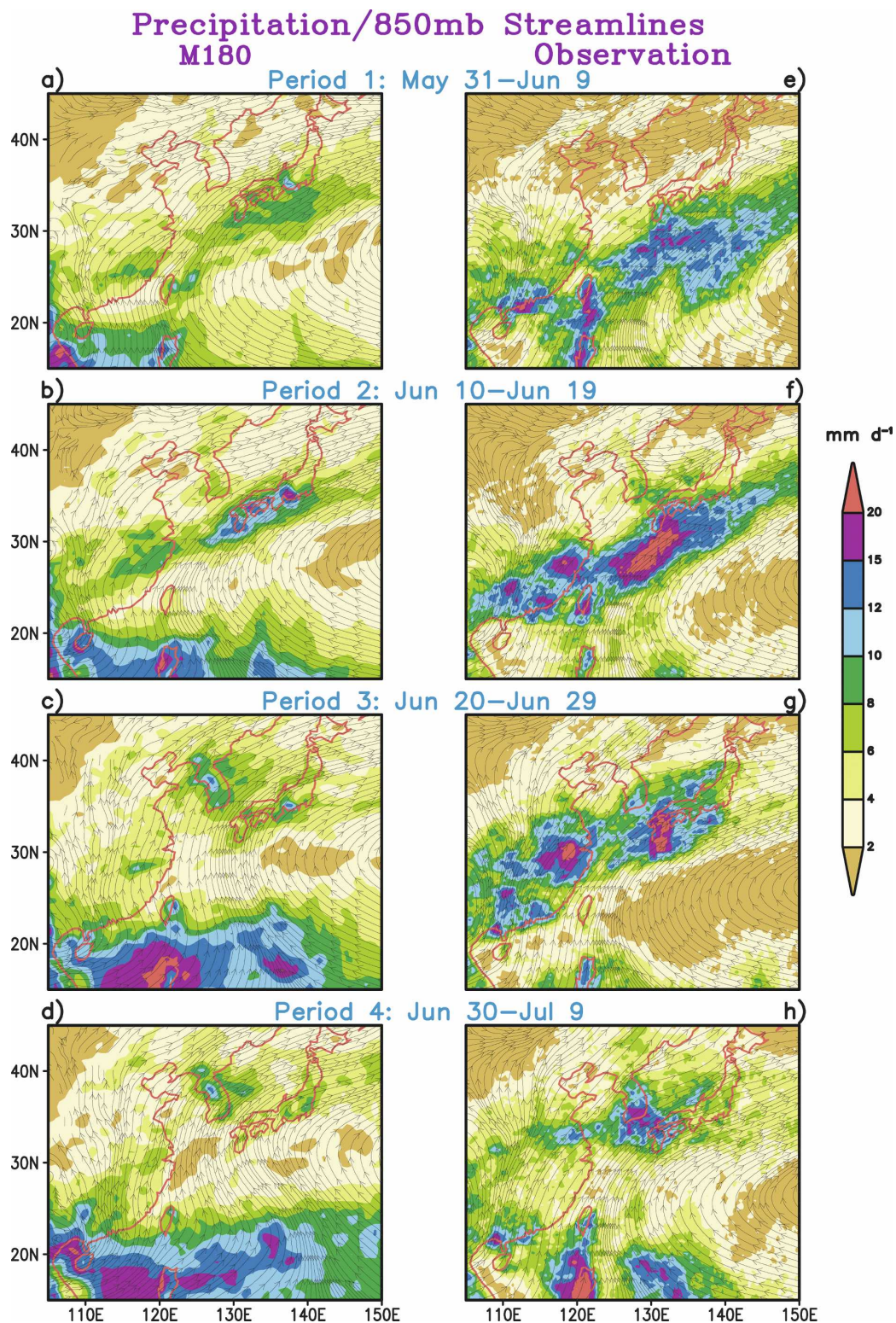
FIG. 6. Distributions of the long-term-averaged precipitation rate (shading, see scale at right) and 850-mb streamlines, as computed using (a)–(d) M180 output and (e)–(h) TRMM/ERA-40 data, for (a), (e) period 1 (31 May–9 Jun); (b), (f) period 2 (10–19 Jun); (c), (g) period 3 (20–29 Jun); and (d), (h) period 4 (30 Jun–9 Jul).
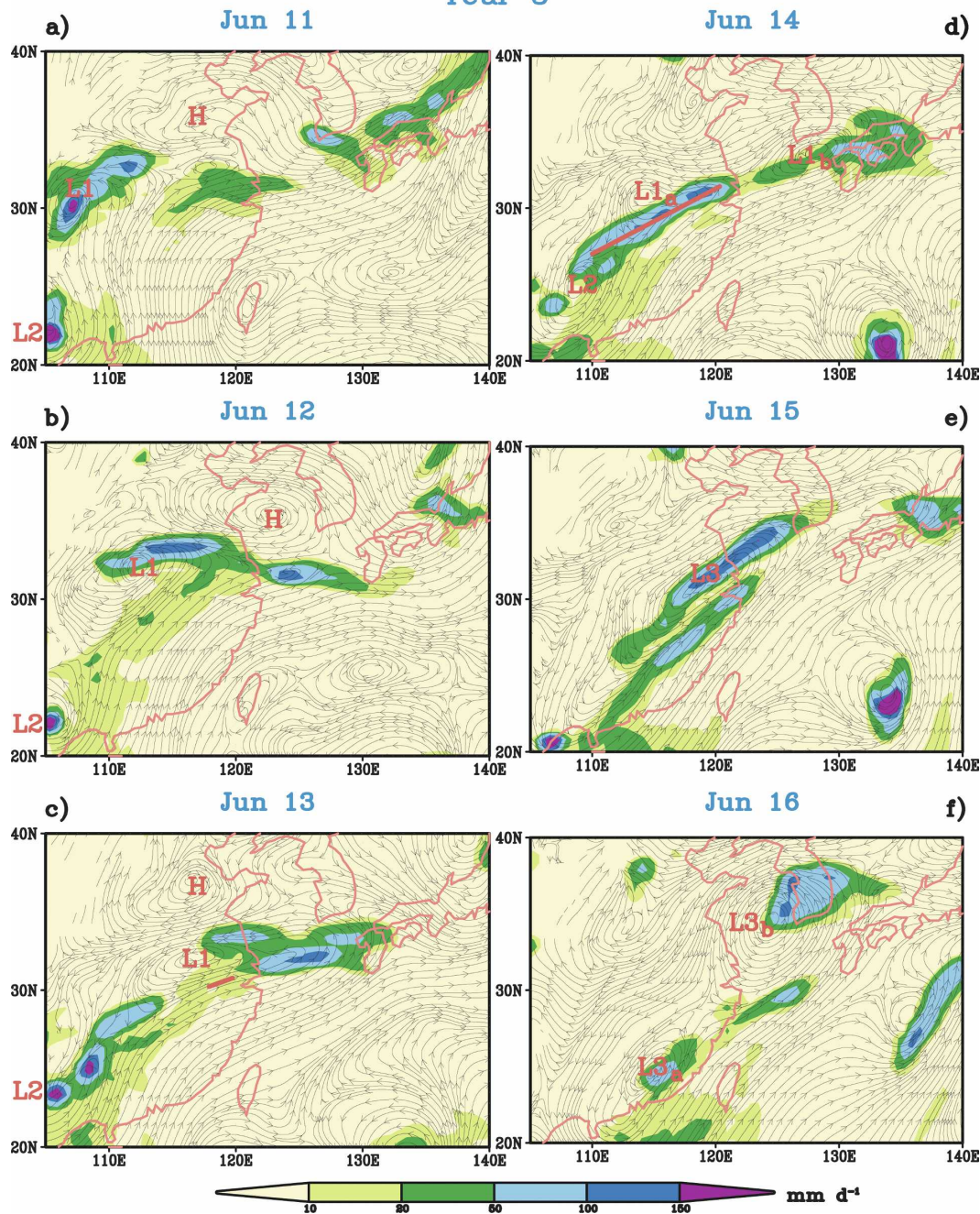
Precipitation/850mb Streamlines
Year 3

FIG. 7. Distributions of the precipitation rate (shading, see scale at bottom) and 850-mb streamlines on individual days of the 11–16 Jun period in year 3 of the M180 integration. Prominent cyclonic and anticyclonic circulation centers are indicated using labels starting with the letters L and H, respectively. Long red line in (d) and short red line in (c) correspond to the segments used for constructing the cross sections in Figs. 9 and 10, respectively.

cyclonic vortex at 850 mb (see labels L1 and L2 in Fig. 7a). During the following two days, L1 migrates continuously eastward as it acquires a more elongated shape with a southwest–northeast orientation. On

11–13 June, a distinct anticyclonic center (see label H in Figs. 7a–c) is situated to the north or northeast of L1. In Fig. 7b, the zone between L1 and H is straddled by easterly flow on its northern flank and southerly or

southwesterly flow to its south, and is thus a site with considerable lateral wind shears and convergence. The most intense precipitation accompanying L1 is located within this zone. On 14 June (Fig. 7d), the cyclonic circulation associated with L1 separates into two centers L1a and L1b, which continue to bring about heavy rainfall over parts of eastern–central China and western Japan, respectively. The vortex L2 moves northeastward on 13–14 June (Figs. 7c,d), and eventually merge with L1a on 15 June to form an elongated trough L3 (Fig. 7e). This broad feature in turn also splits into two distinct centers L3a and L3b, which lead to wet conditions over southeastern coast of China and the southern portion of the Korean Peninsula, respectively.

The general shape and orientation of the simulated rainbands, as shown in Fig. 7, resemble those of the observed mei-yu–baiu systems (Chen 2004; Ninomiya 2004). The alignment of the simulated low-level vorticity cores with the rainbands, the placement of these vortices poleward of the southwesterly airstreams, and the systematic eastward or northeastward movement of both precipitation and vorticity centers, are also in agreement with observations (Ding 1992; Ninomiya 2004). The development of the cyclonic centers L1 and L2 from their incipient stages on 11 June to the mature mei-yu–baiu systems thereafter is similar to the evolution of observed disturbances initiated over the lee slopes of the Tibetan Plateau in southwestern China [referred as the "southwest vortices" by Chinese meteorologists (Ding and Chan 2005)].

The simulated large-scale synoptic environment in which the active mei-yu–baiu systems are embedded is further examined in Fig. 8, which shows the 4-day (11–14 June) averaged distributions of the (Fig. 8a) 500-mb wind speed (shading) and streamlines, and (Fig. 8b) 850-mb temperature (shading) and 500-mb geopotential height (contours). Regions with 4-day-averaged 850-mb wind speeds exceeding 8 m s^{-1} and a precipitation rate exceeding 50 mm day^{-1} are indicated using blue arrows and green shading, respectively.

Within the 100°–130°E sector, the mean background flow in 11–14 June is characterized by a split-jet pattern at 500 mb (Fig. 8a), with one branch located over northern China (40°–45°N) and the other branch over central China (30°N). The midtropospheric circulation over eastern and central China is dominated by a large-scale trough system, whose axis exhibits a distinct southwest–northeast tilt from 30° to 40°N (see green dashed line in Fig. 8a). This spatial shift of the trough axis leads to considerable flow confluence over eastern China and the Yellow Sea near 35°N. The 500-mb flow pattern in the northeastern quadrant of the plotting domain in Fig. 8a is characterized by a trough–ridge–trough wave

train (see labels L, H, and L). Cold air masses reside underneath the two low centers of this wave train (Fig. 8b). At the 850-mb level, a strong southerly airstream is directed from the South China Sea toward southeastern China (see blue arrows in Fig. 8b). It then makes a northeastward turn and traverses over the East China Sea and southern Japan. Precipitation centers (see green shading in Fig. 8b) are simulated along a path lying just to the north of this 850-mb airstream, and southeast of the 500-mb trough over western China (see contours in Fig. 8b). The horizontal scales of the individual rainfall maximum range from 100 to 200 km over southwestern China, to about 300 km over southern Japan.

A schematic sketch of the mei-yu–baiu system has been constructed by Ninomiya (2004) based on observational data (see Fig. 8c). The following observed features in Fig. 8c are in support of the simulated phenomena shown in Figs. 8a,b: two branches of the 500-mb jet stream on the northern and southern perimeters of the Tibetan Plateau (red arrows), which facilitate the propagation of short-wave disturbances; the trough axis over East Asia with a distinct southwest–northeast tilt (dashed black line labeled as "coupled trough"); a chain of low and high centers located poleward of 40°N (labeled as "cold lows" and "blocking ridge"); the southwesterly 850-mb airstream over southeastern China (blue arrows); and a string of mesoscale and synoptic-scale rainbands (labeled as "α" and "S," respectively).

b. Frontal structure

The rainband chosen for this frontal analysis is simulated on 14 June of year 3 (see Fig. 7d), when a coherent belt of almost uniform rain intensity extends over a broad region over central China. The axis of this precipitation zone (hereafter referred to as the "rainband") is indicated in Fig. 7d using a red line segment with a total length of about 1200 km. At various points on this segment, cross sections of various quantities are computed on vertical planes perpendicular to the rainband. These cross sections are oriented from northwest to southeast, and depict spatial distributions as a function of distance normal to the rainband (abscissa) and pressure (ordinate). Altogether 46 such sections are constructed at constant intervals of about 27 km along the rainband. Each section provides a sample of the atmospheric structure in the vicinity of the rainband. Characteristics that are common to all of these sections may be discerned by averaging over all 46 samples the data at a given pressure and distance from the rainband. The patterns thus obtained are displayed in Fig. 9 for (Fig. 9a) temperature T, (Fig. 9b) specific
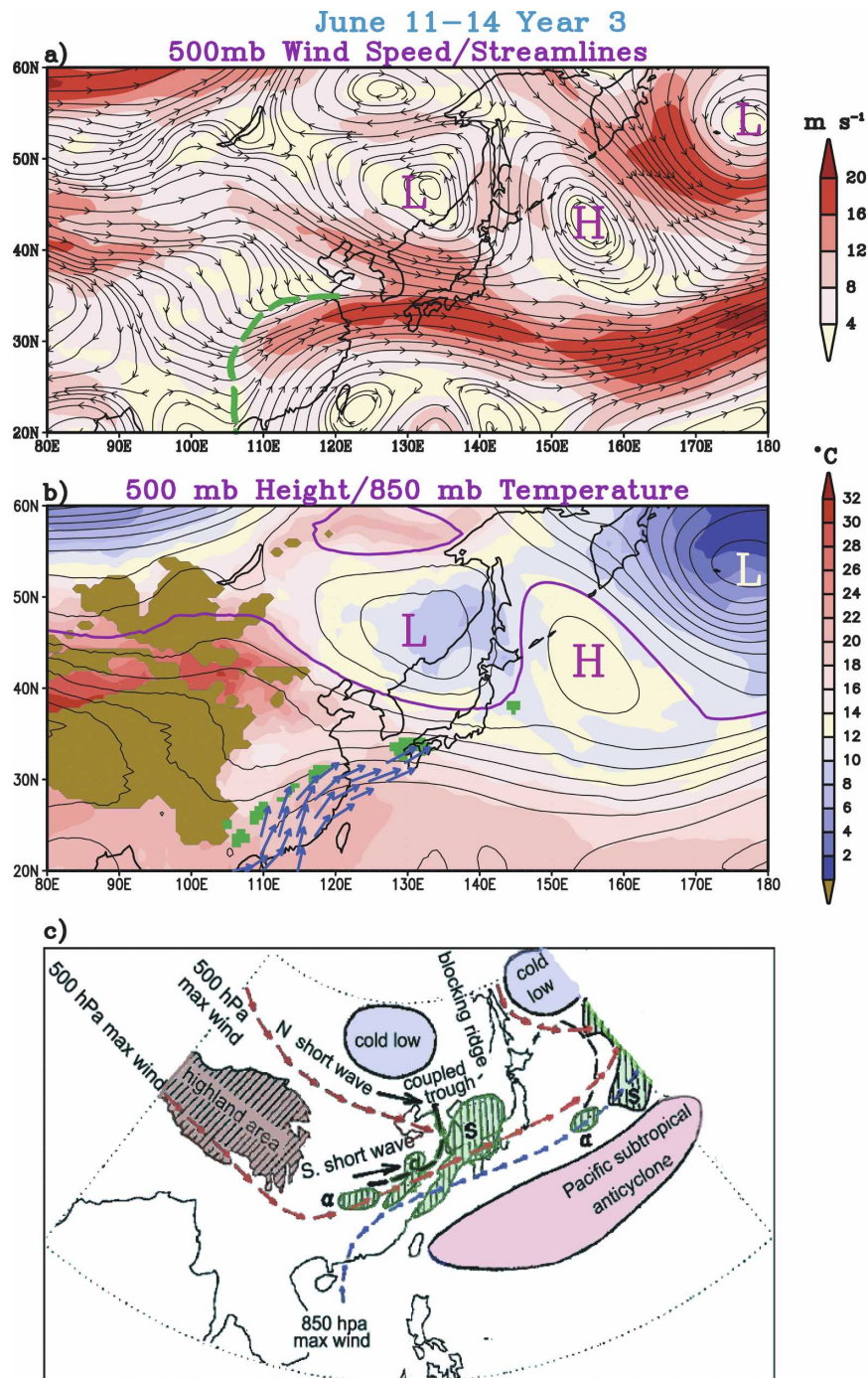
FIG. 8. Distributions of (a) 500-mb wind speed (shading, see scale at right) and streamlines, and (b) 500-mb height (contours; CI: 25 m; 5725-m contour shown in purple) and 850-mb temperature (shading, see scale at right). Cyclonic and anticyclonic centers are highlighted using labels L and H, respectively. In (a), the green dashed line indicates the axis of the tilted 500-mb trough over China. In (b), locations with 850-mb wind speeds exceeding 8 m s^{-1} are indicated using blue arrows; sites with precipitation rates exceeding 50 mm day^{-1} are depicted by green shading; and brown shading denotes regions of high terrain. All data in (a) and (b) are based on averages of the M180 output for the 11–14 Jun period of year 3 in the simulation. Various synoptic features associated with an observed mei-yu–baiu system, as summarized in a schematic fashion by Ninomiya (2004), are shown in (c).
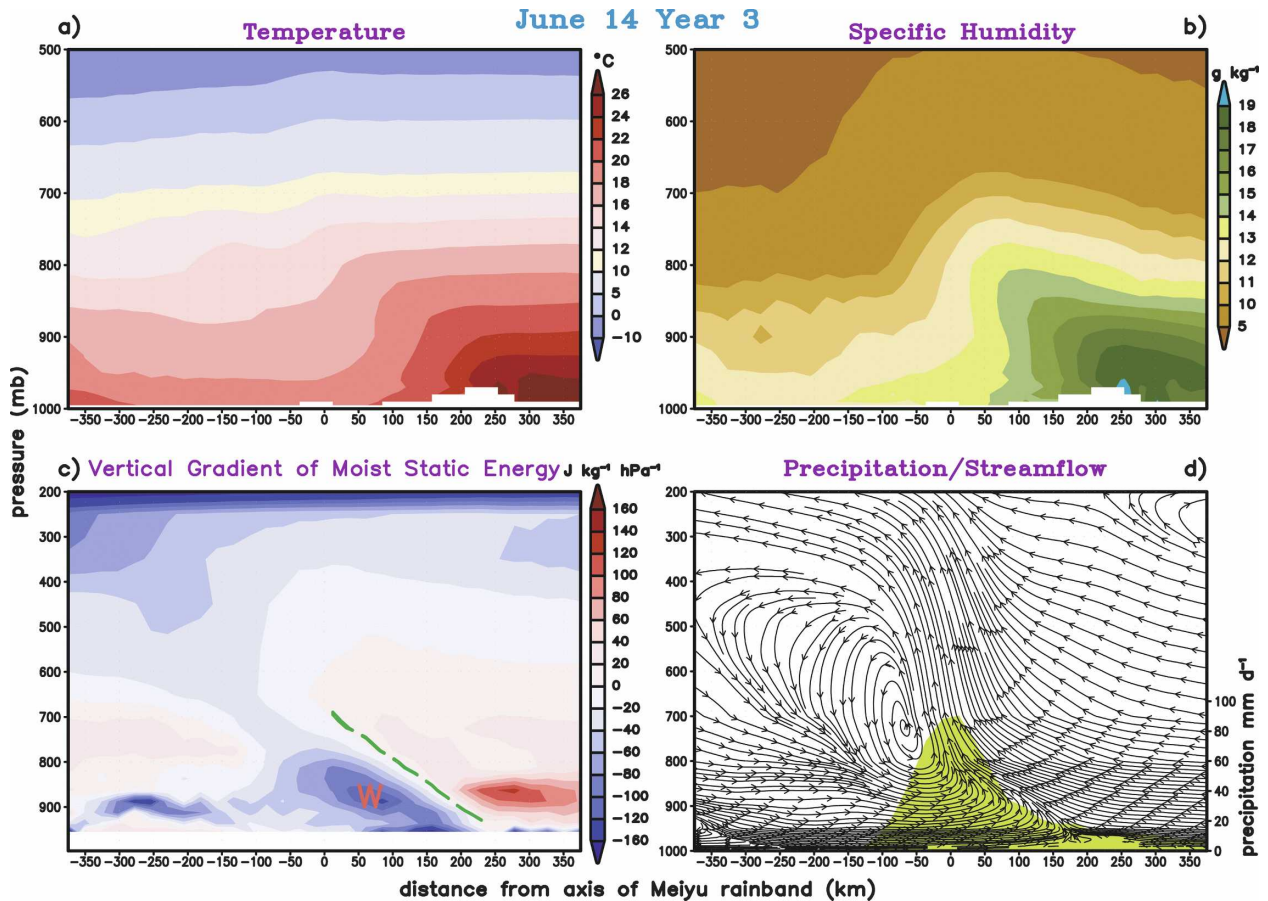
FIG. 9. Cross sections of (a) *T*, (b) *q*, (c) vertical gradient of the moist static energy Δ*h*, and (d) streamflow of the meridional and vertical wind components taken on vertical planes normal to the axis of mei-yu–baiu rainband on 14 Jun of year 3 in the M180 simulation (see red line in Fig. 7d). The ordinate and abscissa correspond to pressure and horizontal distance from the rainband, respectively. Positive and negative values on the abscissa denote distances to the southeast and northwest of the rainband, respectively. The green dashed line in (c) indicate position of the sloping boundary between the stable air mass within the wedgelike feature (denoted by label W, with Δ*h* < 0) and the unstable air mass (with Δ*h* > 0) aloft and to the southeast. Variation of precipitation with distance from the rainband is depicted using the green envelope in (d) and the scale on the right ordinate axis. Note that the upper and lower panels extend vertically to the 500- and 200-mb levels, respectively.

humidity q, (Fig. 9c) the vertical gradient of moist energy, and (Fig. 9d) streamlines depicting vertical and meridional motions. For all panels, the midpoint of the abscissa (labeled as "0") corresponds to the location of the rainband (see red line segment in Fig. 7d). Positive (negative) values along the abscissa correspond to horizontal distances to the southeast (northwest) of the rainband. In Fig. 9c, the moist static energy h is defined as $C_pT + gz + Lq$, where C_p is the specific heat at constant pressure, g is the gravitational acceleration, z is the geopotential height, and L is the latent heat of vaporization. The vertical gradient of h (i.e., $\partial h/\partial p$, hereafter referred to as Δ*h*), which is analogous to the vertical gradient of equivalent potential temperature, is a simple index of atmospheric instability. Positive (negative) values of this quantity indicate an unstable

(stable) atmospheric layer (e.g., see Kemball-Cook and Weare 2001). In Fig. 9d, the variation of precipitation with distance from the rainband is portrayed by green shading, the outline of which corresponds to the precipitation values (see the scale on the right ordinate axis) at various points along the abscissa.

The patterns in Figs. 9a,b portray a thermodynamic structure similar to that of a well-developed weather front, with a warm and moist air mass being situated within the 1000–800-mb layer to the southeast of the precipitation zone, and a distinctly colder and dryer air mass to the northwest of this zone. The juxtaposition of these two air masses leads to strong horizontal gradients in the thermal and moisture fields just to the southeast of the rainband. The maximum near-surface temperature gradient in that region (see Fig. 9a) is ~0.03°C km^{-1},

which is weaker than the corresponding measure ($\sim$0.05°–0.1°C km^{-1}) observed near intense cold fronts in midlatitudes, such as those examined by Kocin et al. (1995). On the other hand, the peak specific humidity gradient seen in Fig. 9b ($\sim$0.03 g kg^{-1} km^{-1}) is stronger than that estimated for the same storm in the observational study cited above ($\sim$0.02 g kg^{-1} km^{-1}).

Because of the presence of high temperature and humidity near the surface of the region located more than 200 km to the southeast of the precipitation zone, the air column over that region is unstable through much of the lower troposphere (Fig. 9c). In contrast, the vertical temperature and humidity profiles at distances of less than 150 km to the southeast of the rainband are characterized by only weak variations with height between 1000 and 800 mb, thus resulting in stable air columns over that zone (Fig. 9c). The boundary between this stable region and the unstable region to its southeast (see green dashed line in Fig. 9c) is seen to slant northwestward with increasing height. The stable region hence has the characteristic shape of a wedge, which "undercuts" the unstable air lying aloft and to the southeast. Analogous cross sections of $\partial C_p T/\partial p$ and $\partial Lq/\partial p$ separately (not shown) indicate that the vertical profile of q plays a more important role than the profile of T in determining the stability characteristics within the 750–1000-mb layer.

The precipitation profile (green envelope in Fig. 8d) is characterized by a distinct peak centered at the axis of the rainband. Below the 800-mb level, northerly (southerly) flow prevails in the sector northwest (southeast) of the rainband. The northerly flow is seen to penetrate beyond the axis of the rainband. The spatial extent of this "overshooting" tendency is largest at the surface, where northerly flow is discernible as far as 175 km southeastward of the rainband. The degree of penetration is seen to diminish gradually above the ground level, so that the boundary between the low-level northerly and southerly flows slopes northwestward with increasing altitude. This boundary is situated near the surface of the wedgelike region of moist static stability noted in Fig. 9c (see dashed green line in that panel). The northward moving air in the lower troposphere of the southeastern sector is seen to glide over this wedge, and then rises through the mid- and upper troposphere over the precipitation zone. The upper-level flow pattern in the northwestern sector is dominated by a circulation cell with ascending motion over the rainband, northward flow above the 500-mb level, and descending motion at distances beyond 150 km to the northwest of the rainband.

The model results in Fig. 9 may be compared with the corresponding features of typical mei-yu–baiu fronts based on observations, as presented schematically by Liu et al. (2003) and reproduced in the review by Ding and Chan (2005, see their Fig. 15), and by Chen and Hui (1990, see their Fig. 19). Many aspects of the model simulation are supported by observational evidence. In particular, the observed mei-yu–baiu rainband is associated with a frontal boundary that slopes poleward with increasing height. As in the model atmosphere, the observed circulation is characterized by the overrunning above this frontal surface of warm and moist air with tropical origin, and the undercutting of cold air underneath.

To further diagnose the dynamical processes associated with the flow component parallel to the mei-yu–baiu rainband, cross sections analogous to those in Fig. 9 have been constructed using data for 13 June with reference to a shorter segment near 30°N, 120°E (see bold red line in Fig. 7c). This segment is selected by virtue of its collocation with the axis of a distinct wind speed maximum at 700 mb on that date (figure not shown), and is hereafter referred to as the low-level wind (LLW) axis. At five points along this LLW axis (with a constant interval of about 27 km), cross sections are taken along vertical planes that are oriented normal to the axis, and the averages over this set of five cross sections are then computed. This analysis procedure is analogous to that used in constructing Fig. 9. The resulting distributions of the speed of the wind component parallel to the LLW axis (contours) and horizontal flow divergence (shading) are presented in Fig. 10a. Sites of maximum rising motion are indicated using green arrows. Variation of precipitation as a function of distance from the LLW axis is shown in Fig. 10b. Values on the abscissa show distances from the LLW axis, and are positive (negative) for points located to the southeast (northwest) of this axis.

Over the region situated within 600 km to the southeast of the line segment, the vertical profile of the strength of the northeastward flow (as indicated by solid contours in Fig. 10a) is characterized by increasing wind speeds with height in the lower troposphere, and decreasing wind speeds with height in the mid- and upper troposphere. The site of maximum wind strength (see the label "J_L^+" in Fig. 10a) is located at about 700 mb near the LLW axis (i.e., midpoint of the abscissa). The red dashed line, which links the wind speed maxima at various altitudes, is seen to slope downward to the 950-mb level with increasing distance from the LLW axis. The appearance of this intensified flow in the lower layers of the model atmosphere is reminiscent of the low-level jets that are often observed in the vicinity of mei-yu–baiu systems (e.g., see Ding 1992; Chen 2004). The amplitude of the simulated jet maxi-
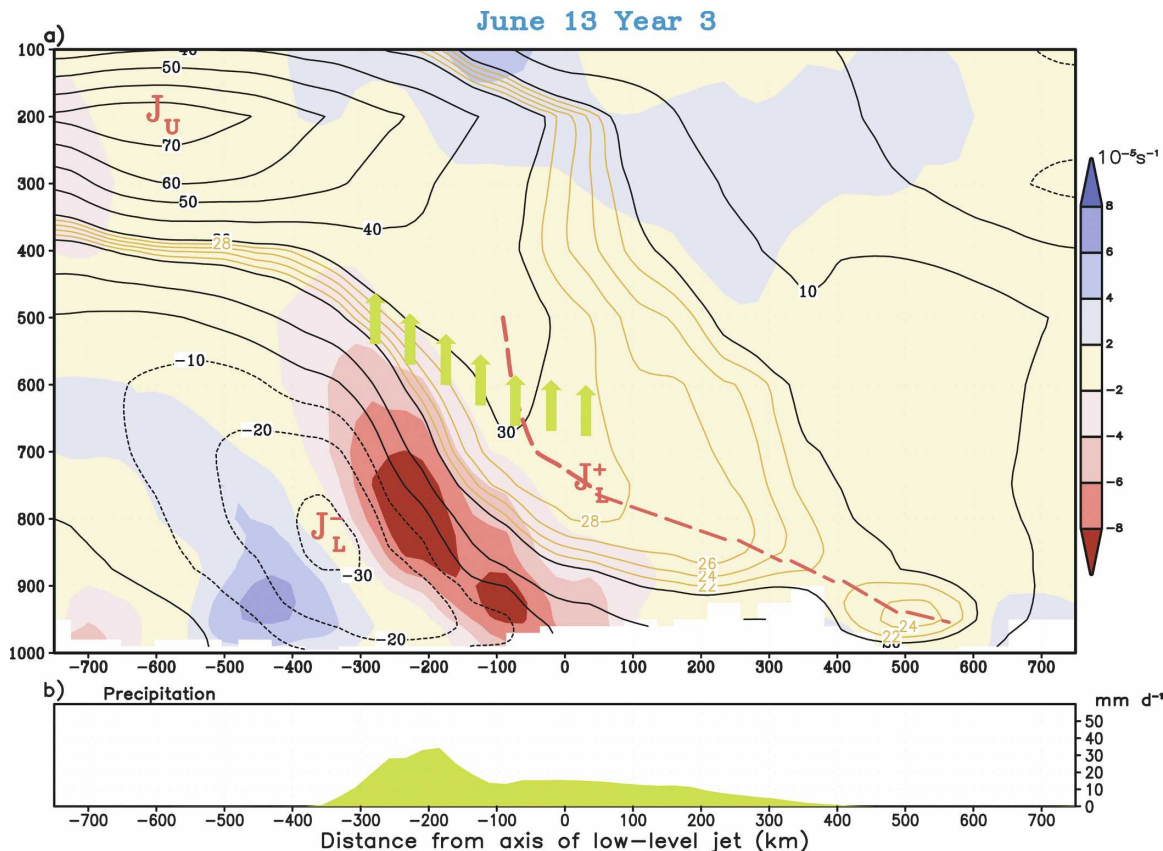
FIG. 10. (a) Cross section of the speed of the wind component parallel to the LLW axis, as depicted by the short red line segment in Fig. 7c (contours; CI: 2 m s^{-1} between 20 and 30 m s^{-1}; 10 m s^{-1} otherwise) and horizontal divergence (shading, see scale at right), taken on vertical planes normal to the LLW axis. Positive wind speed values denote flows that are oriented northeastward, i.e., pointing into the plane of (a). Negative wind speed values represent southwestward flows that are directed out of the plane of (a). The ordinate and abscissa correspond to pressure and horizontal distance from the LLW axis, respectively. Positive and negative values on the abscissa denote distances to the southeast and northwest of the LLW axis, respectively. Locations of maxima in upward motion are indicated using green arrows. Positions of jetlike features are denoted by labels J_L^+, J_L^-, and J_U. The axis of maximum strength of the northeastward flow in the lower troposphere is depicted by the red dashed line. (b) Variation of precipitation with distance from the LLW axis. All results are based on data for 13 Jun in year 3 of the M180 simulation. Note that the range of the abscissa in this figure is 2 times longer than that in Fig. 9.

mum (20–30 m s^{-1}) and its vertical placement are also in agreement with observations. Over the region to the northwest of the LLW axis, the flow structure is dominated by the southwesterly jet (labeled as "J_U") located at 200 mb and about 600 km from the axis, and strong northeasterly flows (J_L^-) with a distinct core (see negative extremum in Fig. 10a) centered at 900–800 mb and 350 km from the axis.

The 850-mb cyclone L1 on 13 June (Fig. 7c) is straddled by J_L^+ and J_L^- (Fig. 10a). Low-level horizontal convergence (note red shading in Fig. 10a) is seen to prevail in the vicinity of this site. The resulting positive vorticity tendencies would further increase the cyclonic flow associated with L1. By the same token, the negative vorticity changes induced by horizontal divergence on the southeastern flank of the upper-level jet stream

J_U (blue shading in Fig. 10a) lead to strengthening of the anticyclonic shear in that region. This convergence–divergence couplet is accompanied by rising motion (see green arrows) and enhanced precipitation (green envelope in Fig. 10b) over the sector within 300 km to the northwest of the LLW axis. The locations of the maxima in both low-level convergence and vertical velocity slope upward with increasing distance to the northwest of the LLW axis.

As portrayed in Fig. 10, the precipitation maximum is sandwiched between the low-level jetlike feature J_L^+ (which is situated near the midpoint of the abscissa) and the upper-level jet stream J_U (which is located at about 700 km to the northwest of J_L^+). These spatial relationships between the simulated mei-yu–baiu rainband and the three-dimensional ambient flow pattern

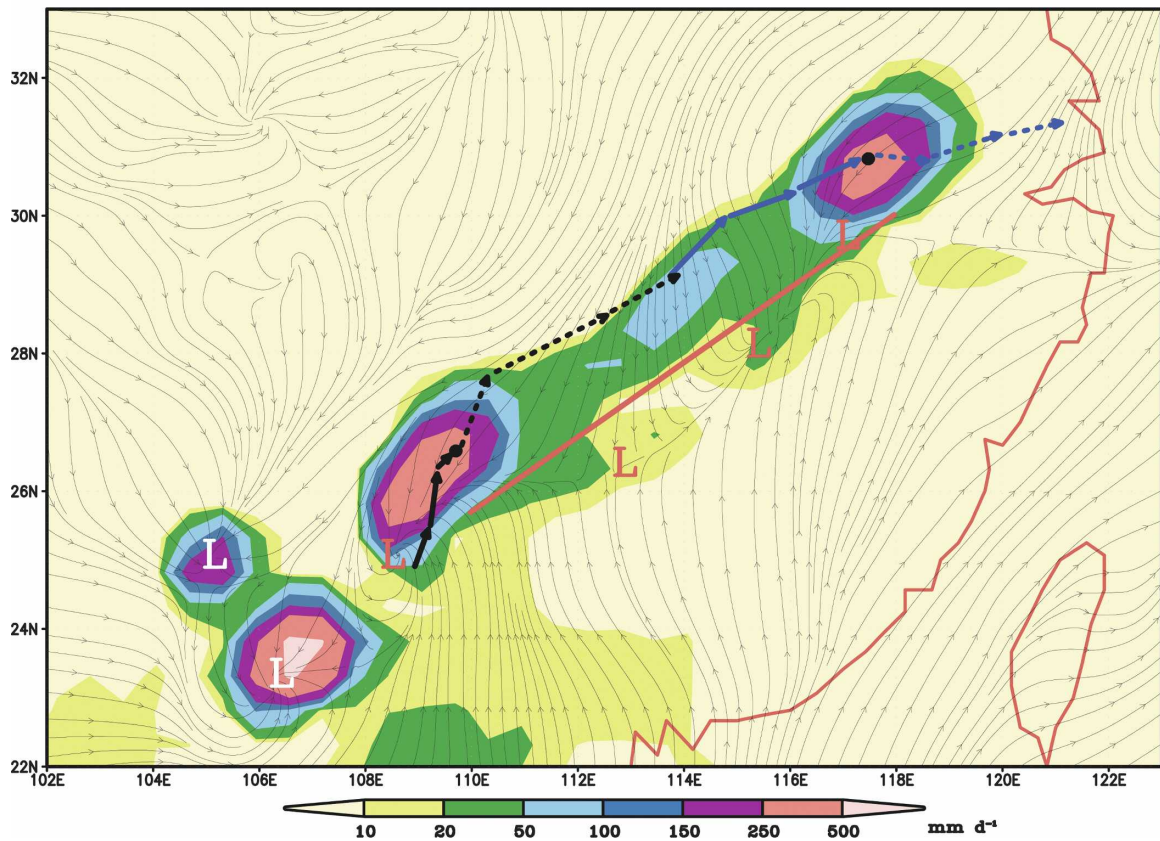## Precipitation/Surface Streamlines
00Z June 14 Year 3

FIG. 11. Distribution of the precipitation rate during the 3-h period prior to 0000 UTC 14 Jun in year 3 of the M180 simulation (shading, see scale at bottom), and the surface streamflow pattern at 0000 UTC of the same date. Locations of the two principal precipitation centers along the elongated mei-yu–baiu rainband at 0000 UTC are denoted by black dots. The trajectory of each center during the 18-h period from 1500 UTC 13 Jun to 0900 UTC 14 Jun is shown using a set of 3-h displacement vectors (arrows with solid and dashed shafts correspond to movements before and after 0000 UTC, respectively). Axis of maximum horizontal gradients of surface air temperature is indicated by the red line. Positions of low centers in the surface pressure field are depicted by the labels L.

are consistent with those deduced from observations, as noted by Ding (1992, see his Fig. 10).

c. Synoptic environment and propagation characteristics of precipitation centers

The evolution of precipitation extrema and their synoptic environment on subdaily time scales in the above model episode is examined by mapping the model fields at 3-hourly intervals. The distribution of the rainfall rate during the 3-h period ending at 0000 UTC 14 June of year 3 of the M180 simulation is shown in Fig. 11 using shading. The streamline pattern at 10 m above the lower model surface at 0000 UTC is also displayed in this figure. The principal low pressure centers are indicated using the labels "L." The zone of strongest horizontal gradients in surface air temperature is depicted

by the red line segment. The migratory path of two selected rainfall maxima embedded in the main mei-yu–baiu system (see black dots) is portrayed in Fig. 11 by a set of arrows connecting the sites of the maximum in successive 3-hourly time steps from 1500 UTC 13 June to 0900 UTC 14 June.

The precipitation maxima appearing in Fig. 11 (based on rainfall accumulation over a 3-h period) are more distinct and have considerably higher amplitudes than those seen in Fig. 7d (based on accumulation over 24 h). Each precipitation center in Fig. 11 is associated with a well-organized depression in the surface pressure field (denoted by L) and surface flow convergence (see streamline pattern), and have a typical horizontal scale of 100–200 km. The strongest horizontal gradients of surface air temperature are located to the south of the axis of the main mei-yu–baiu rainband (see red line).

Northerly surface flows prevail beneath almost the entire length of main mei-yu–baiu rainband. A well-defined convergence zone is established on the equatorward flank of this rainband.

The trajectories of the two precipitation centers within the mei-yu–baiu rainhand in the 18-h duration centered at 0000 UTC (see solid and dashed arrows in Fig. 11) have a general southwest–northeast orientation, and are mostly parallel to the axis of the rainband as well as the zone of strong temperature gradients. The typical propagation speed of these rainfall maxima, as inferred from the distances traveled during the 18-h period considered here, is approximately 12 m s^{-1}. This value is in good agreement with the corresponding observational estimate (Ninomiya 2004).

d. Other examples of mei-yu–baiu systems

In addition to the outstanding case of mei-yu–baiu development in mid-June of year 3, rainy episodes with similar characteristics can be identified in the May–July period of many other years in the model simulation. The typical duration of these episodes is approximately 5–10 days. Three examples of these mei-yu–baiu rainbands (shading) and the ambient 850-mb flow field (streamlines) on selected dates in years 4, 8, and 9 are displayed in Fig. 12. In all three events, heavy precipitation is generated over an elongated zone near the Yangtze River basin of central China, with a southwest-to-northeast orientation. These rainbands are straddled by low-level southwesterly flow to its south, and northeasterly flow to its north. Many of the individual precipitation maxima are accompanied by distinctive cyclonic centers or troughlike circulations. The appearance of these common features in multiple episodes confirms that the mei-yu–baiu rainband is a recurrent phenomenon in the model atmosphere.

6. Summary and discussion

The simulation of various climatological and synoptic aspects of the Asian summer monsoon system by a global atmospheric GCM with a horizontal resolution of about 50 km is examined, with particular emphasis on fine structures with scales that are comparable to that of the model grid. Our investigation begins with an overview of the AM simulations by different model versions, the spatiotemporal evolution of various regional components of the continental-scale monsoon circulation, and the corresponding seasonal march of the principal heat sources and sinks (section 3). Attention is then focused on the unique monsoon features in the East Asian sector. It is demonstrated that the precipi-

tation pattern in that region is closely related to the behavior of elongated, southwest–northeast-oriented mei-yu–baiu rainbands. Climatological data with pentadal resolution reveal that the simulated mei-yu–baiu systems typically make a sequence of jumps from ~25° to ~40°N during the May–July period (section 4). The advances of these rainbands from the subtropics to higher latitudes are accompanied by systematic shifts in the axis of the western Pacific anticyclone.

An in-depth analysis has been performed on an outstanding case of mei-yu–baiu development in the model atmosphere, so as to study the synoptic and mesoscale characteristics of this phenomenon (section 5). During this week-long episode, the persistent heavy precipitation over the Yangtze River basin is coincident with the passage of a succession of cyclonic centers, which are clearly identifiable on daily and subdaily time scales. These disturbances are steered by the enhanced midtropospheric flow in that region. Moisture is supplied to this rainbelt by low-level southerly airstreams originating from the South China Sea. Cross sections normal to the axis of the rainband reveal thermodynamic and circulation characteristics that are similar to those observed in midlatitude weather fronts, except that the moisture gradients near the mei-yu–baiu fronts are relatively stronger. Straddling of the precipitation maximum by a jetlike feature at low levels and the principal jet core near the tropopause is seen to be dynamically consistent with the patterns of divergence and vertical motion associated with this flow environment.

Whenever feasible, the model results described above are compared with observational data. Special attention is devoted to the fidelity of the simulation of atmospheric features with scales approaching the resolution limit of the model. Examples of such small-scale aspects of model behavior include the monsoon rains near the Western Ghats of India, the southern slopes of the Tibetan Plateau, and the mei-yu–baiu system (Fig. 2); the poleward displacements of the mei-yu–baiu rainband and the western Pacific subtropical anticyclone in successive pentads (Figs. 5–6); the detailed thermodynamic and circulation structure of the mei-yu–baiu front (Figs. 9–10); and propagation behavior of mesoscale vortices along the mei-yu–baiu rainband (Fig. 11). Obviously, such diagnoses would not have been possible with output from a model with coarser resolution.

Whereas it is illustrated that the M180 model is capable of reproducing many mesoscale characteristics of the mei-yu–baiu fronts (section 5), several discrepancies between model and observations in regards to the climatological aspects of these systems are also noted (section 4). In particular, the northward advance of the
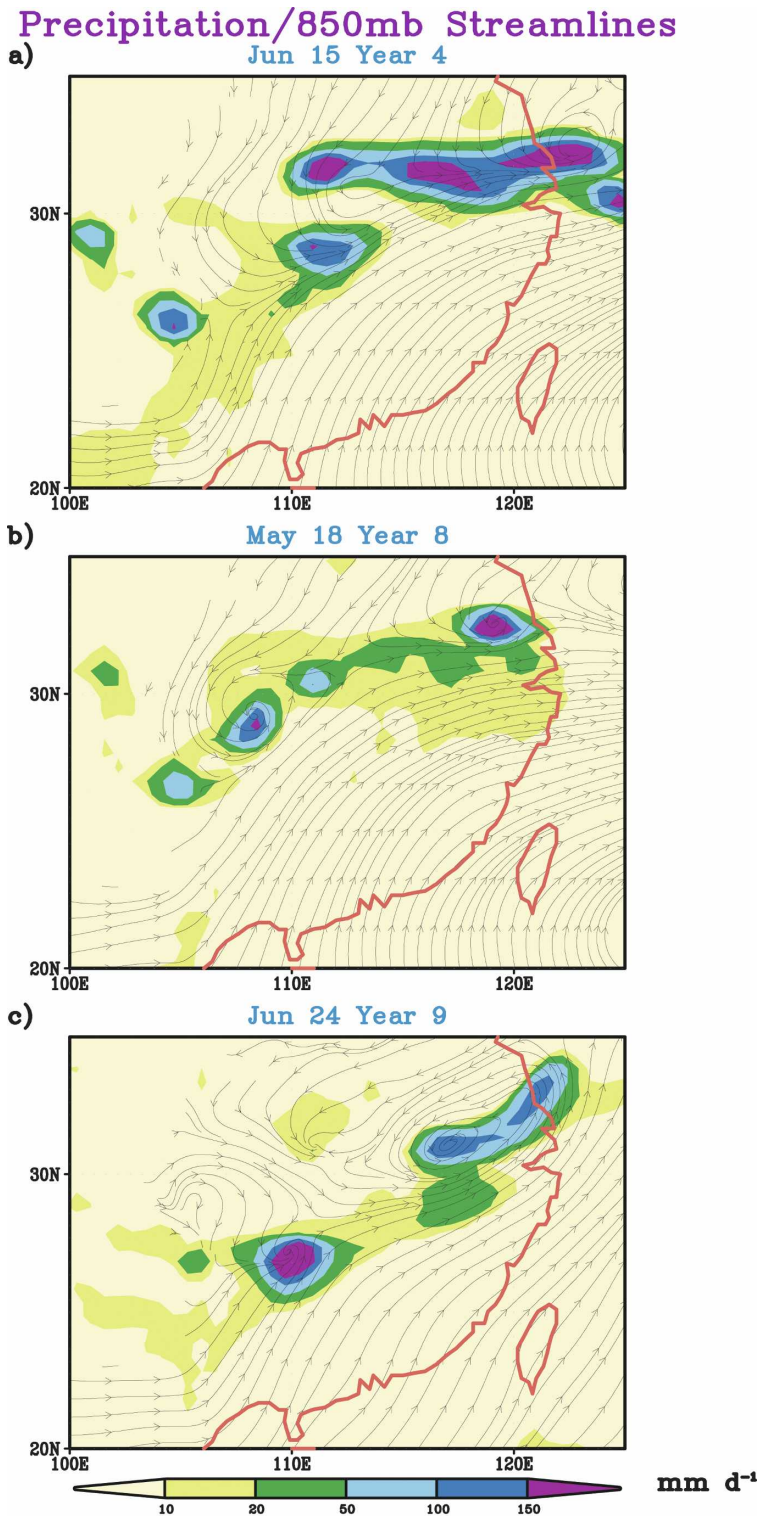
Precipitation/850mb Streamlines

FIG. 12. Distributions of precipitation rates (shading, see scale at bottom) and 850-mb streamlines on three other dates with strong mei-yu–baiu development in the M180 simulation: (a) 15 Jun of year 4, (b) 18 May of year 8, and (c) 24 Jun of year 9.

long-term-averaged precipitation zone proceeds earlier in the model than in the observed atmosphere by approximately two pentads. The observed maximum climatological rainfall rate within this zone (exceeding 15 mm day^{-1}) is higher than the model values (mostly less than 10 mm day^{-1}). This underestimation of the climatological precipitation rate in the mei-yu–baiu region is evident in model versions with a broad range of resolutions (see Fig. 1). The enhanced ability of the higher-resolution versions (M360 or M180) to capture the detailed characteristics of the mei-yu–baiu circulation features does not yield an improved rainfall climatology as compared with the M90 or M45 simulations (see Figs. 1b–e). For the M180 version, the mei-yu–baiu rainband is less organized in its latter phases of development (late June–early July) than the TRMM patterns (cf. Figs. 6c,d with Figs. 6g,h). Additional diagnoses are needed to identify the causes for the above model deficiencies, and to delineate the mechanisms contributing to the stepwise character of the poleward jumps of the simulated mei-yu–baiu rainbelts on time scales of approximately 10–15 days.

Comparison of a variety of simulated small-scale features with available observations serves as a stringent test of the capacity of the high-resolution climate models in reproducing the full range of atmospheric phenomena. Some of the subsynoptic-scale systems play a substantial role in both the long-term-averaged and time-varying states of regional climates. For instance, it is estimated from climatological statistics that as much as 40% of the observed summertime heavy rain events over the Yangtze River basin occur within the mei-yu–baiu period from mid-June to mid-July (Ding 1992); and severe droughts and floods in that region are closely related to interannual and intraseasonal changes in the intensity and locality of the mei-yu–baiu rainbands. Demonstration of the realistic representation of such weather disturbances in high-resolution GCMs would therefore enhance our confidence in applying such model tools for understanding and projecting detailed local manifestations of large-scale variability and climate change.

This study is primarily devoted to the diagnosis of phenomena related to the EASM, which comprise only a small subset of the circulation systems occurring throughout the globe. For a complete assessment of the performance of high-resolution GCMs in simulating various facets of the monsoon flow, the scope of this work needs to be broadened considerably, so as to cover meteorological features occurring in various monsoon regions beyond East Asia, and in all phases of the annual cycle. An even more comprehensive evalu-

ation of model fidelity would entail examination of the myriad phenomena prevailing outside of the monsoon regions, such as convective structures in the deep tropics and baroclinic systems in mid- and high-latitude zones.

REFERENCES

Branković, Č., and D. Gregory, 2001: Impact of horizontal resolution on seasonal integrations. *Climate Dyn.,* **18,** 123–143.

Chang, C.-P., Ed., 2004: *East Asian Monsoon.* Vol. 2, *World Scientific Series on Meteorology of East Asia,* World Scientific, 564 pp.

Chen, G. T.-J., 2004: Research on the phenomena of Meiyu during the past quarter century: An overview. *East Asian Monsoon,* C.-P. Chang, Ed., Vol. 2, *World Scientific Series on Meteorology of East Asia,* World Scientific, 357–403.

Chen, Y.-L., and N. B.-F. Hui, 1990: Analysis of a shallow front during the Taiwan Area Mesoscale Experiment. *Mon. Wea. Rev.,* **118,** 2649–2667.

Copsey, D., R. Sutton, and J. R. Knight, 2006: Recent trends in sea level pressure in the Indian Ocean region. *Geophys. Res. Lett.,* **33,** L19712, doi:10.1029/2006GL027175.

Delworth, T. L., and Coauthors, 2006: GFDL's CM2 global coupled climate models. Part I: Formulation and simulation characteristics. *J. Climate,* **19,** 643–674.

Ding, Y., 1992: Summer monsoon rainfalls in China. *J. Meteor. Soc. Japan,* **70,** 373–396.

——, 2004: Seasonal march of the East-Asian summer monsoon. *East Asian Monsoon,* C.-P. Chang, Ed., Vol. 2, *World Scientific Series on Meteorology of East Asia,* World Scientific, 30–53.

——, and J. C. L. Chan, 2005: The East Asian summer monsoon: An overview. *Meteor. Atmos. Phys.,* **89,** 117–142.

Duffy, P. B., B. Govindasamy, J. P. Iorio, J. Milovich, K. R. Sperber, K. E. Taylor, M. F. Wehner, and S. L. Thompson, 2003: High-resolution simulations of global climate, Part 1: Present climate. *Climate Dyn.,* **21,** 371–390.

Fu, X., B. Wang, and T. Li, 2002: Impacts of air–sea coupling on the simulation of mean Asian summer monsoon in the ECHAM4 model. *Mon. Wea. Rev.,* **130,** 2889–2904.

Gadgil, S., and K. Rupa Kumar, 2006: The Asian monsoon—Agriculture and economy. *The Asian Monsoon,* B. Wang, Ed., Springer-Praxis, 651–683.

GFDL Global Atmospheric Model Development Team, 2004: The new GFDL global atmosphere and land model AM2–LM2: Evaluation with prescribed SST simulations. *J. Climate,* **17,** 4641–4673.

Huffman, G. J., and Coauthors, 2007: The TRMM Multisatellite Precipitation Analysis (TMPA): Quasi-global multiyear, combined-sensor precipitation estimates at fine scales. *J. Hydrometeor.,* **8,** 38–55.

Kang, I.-S., 2004: Current status of AGCM monsoon simulations. *East Asian Monsoon,* C.-P. Chang, Ed., Vol. 2, *World Scientific Series on Meteorology of East Asia,* World Scientific, 301–331.

——, and Coauthors, 2002: Intercomparison of the climatological variations of Asian summer monsoon precipitation simulated in 10 GCMs. *Climate Dyn.,* **19,** 383–395.

Katayama, A., 1967: On the radiation budget of the troposphere over the northern hemisphere (III). Zonal cross-section and energy consideration. *J. Meteor. Soc. Japan,* **45,** 26–39.

Kikuchi, K., and B. Wang, 2008: Diurnal precipitation regimes in the global tropics. *J. Climate,* **21,** 2680–2696.

Kemball-Cook, S. R., and B. C. Weare, 2001: The onset of convection in the Madden–Julian Oscillation. *J. Climate,* **14,** 780–793.

Kocin, P. J., P. N. Schumacher, R. F. Morales Jr., and L. W. Uccellini, 1995: Overview of the 12–14 March 1993 superstorm. *Bull. Amer. Meteor. Soc.,* **76,** 165–182.

Kummerow, C., and Coauthors, 2000: The status of the Tropical Rainfall Measuring Mission (TRMM) after two years in orbit. *J. Appl. Meteor.,* **39,** 1965–1982.

Lau, K.-M., and M. T. Li, 1984: The monsoon of East Asia and its global associations—A survey. *Bull. Amer. Meteor. Soc.,* **65,** 114–125.

——, G. J. Yang, and S. Shen, 1988: Seasonal and intraseasonal climatology of summer monsoon rainfall over East Asia. *Mon. Wea. Rev.,* **116,** 18–37.

——, J. H. Kim, and Y. Sud, 1996: Intercomparison of hydrologic processes in AMIP GCMs. *Bull. Amer. Meteor. Soc.,* **77,** 2209–2227.

Lin, S.-J., 2004: A "vertically Lagrangian" finite-volume dynamical core for global models. *Mon. Wea. Rev.,* **132,** 2293–2307.

LinHo, V., X. Huang, and N.-C. Lau, 2008: Winter-to-spring transition in East Asia: A planetary-scale perspective of the South China Spring Rain Onset. *J. Climate,* **21,** 3081–3096.

Liu, J. J., Y. H. Ding, and J. H. He, 2003: The structure analysis of a typical Meiyu front. *Acta Meteor. Sin.,* **61,** 291–301.

Luo, H., and M. Yanai, 1984: The large-scale circulation and heat sources over the Tibetan Plateau and surrounding areas during the early summer of 1979. Part II: Heat and moisture budgets. *Mon. Wea. Rev.,* **112,** 966–989.

Mizuta, R., and Coauthors, 2006: 20-km-mesh global climate simulations using JMA-GSM model—Mean climate states. *J. Meteor. Soc. Japan,* **84,** 165–185.

Moorthi, S., and M. J. Suarez, 1992: Relaxed Arakawa–Schubert: A parameterization of moist convection for general circulation models. *Mon. Wea. Rev.,* **120,** 978–1002.

Ninomiya, K., 2004: Large- and mesoscale features of Meiyu-Baiu front associated with intense rainfalls. *East Asian Monsoon,* C.-P. Chang, Ed., Vol. 2, *World Scientific Series on Meteorology of East Asia,* World Scientific, 404–435.

Nitta, T., 1983: Observational study of heat sources over the eastern Tibetan Plateau during the summer monsoon. *J. Meteor. Soc. Japan,* **61,** 590–605.

Ohfuchi, W., and Coauthors, 2004: 10-km mesh meso-scale resolving simulations of the global atmosphere on the Earth Simulation—Preliminary outcomes of AFES (AGCM for the Earth Simulator). *J. Earth Simulator,* **1,** 8–34.

Reynolds, R. W., N. A. Rayner, T. M. Smith, D. C. Stokes, and W. Wang, 2002: An improved in situ and satellite SST analysis for climate. *J. Climate,* **15,** 1609–1625.

Roeckner, E., and Coauthors, 2006: Sensitivity of simulated climate to horizontal and vertical resolution in the ECHAM5 atmosphere model. *J. Climate,* **19,** 3771–3791.

Sperber, K. R., and T. N. Palmer, 1996: Interannual tropical rainfall variability in general circulation model simulations associated with the Atmospheric Model Intercomparison Project. *J. Climate,* **9,** 2727–2750.

——, S. Hameed, G. L. Potter, and J. S. Boyle, 1994: Simulation of the northern summer monsoon in the ECMWF model: Sensitivity to horizontal resolution. *Mon. Wea. Rev.,* **122,** 2461–2481.

Trenberth, K. E., J. W. Hurrell, and D. P. Stepaniak, 2006: The Asian monsoon: Global perspectives. *The Asian Monsoon,* B. Wang, Ed., Springer-Praxis, 67–87.

Ueda, H., H. Kamahori, and N. Yamazaki, 2003: Seasonal contrasting features of heat and moisture budgets between the eastern and western Tibetan Plateau during the GAME IOP. *J. Climate,* **16,** 2309–2324.

Uppala, S. M., and Coauthors, 2005: The ERA-40 re-analysis. *Quart. J. Roy. Meteor. Soc.,* **131,** 2961–3012.

Wang, B., Ed., 2006: *The Asian Monsoon.* Spring-Praxis, 787 pp.

——, and X. Xu, 1997: Northern Hemisphere summer monsoon singularities and climatological intraseasonal oscillation. *J. Climate,* **10,** 1071–1085.

——, I.-S. Kang, and J.-Y. Lee, 2004: Ensemble simulations of Asian–Australian monsoon variability by 11 AGCMs. *J. Climate,* **17,** 803–818.

Yanai, M., and G.-X. Wu, 2006: Effects of the Tibetan Plateau. *The Asian Monsoon,* B. Wang, Ed., Springer-Praxis, 513–549.

Yeh, T.-C., and Y.-X. Gao, 1979: *The Meteorology of the Qinghai-Xizang (Tibet) Plateau* (in Chinese). Science Press, 278 pp.